Smoking and tetramer tryptase accelerate intervertebral disc degeneration by inducing METTL14-mediated *DIXDC1* m^6 modification

Ji Tu,[1] Wentian Li,[1] Philip M. Hansbro,[2,3] Qi Yan,[4] Xupeng Bai,[5,6] Chantal Donovan,[2,3] Richard Y. Kim,[2,3] Izabela Galvao,[2,3] Abhirup Das,[1] Cao Yang,[7] Jun Zou,[4] and Ashish Diwan[1,8]

[1]Spine Labs, St. George & Sutherland Clinical School, Faculty of Medicine, University of New South Wales, Sydney, NSW, Australia; [2]Faculty of Science, School of Life Sciences, Centre for Inflammation, Centenary Institute, University of Technology Sydney, Sydney, NSW, Australia; [3]Priority Research Centre for Healthy Lungs, Hunter Medical Research Institute, University of Newcastle, Newcastle, NSW, Australia; [4]Department of Orthopedic Surgery, The First Affiliated Hospital of Soochow University, Suzhou, China; [5]Center for Innovation and Translational Medicine, First Affiliated Hospital, Zhejiang University School of Medicine, Hangzhou, China; [6]Zhejiang Provincial Key Laboratory of Pancreatic Disease, First Affiliated Hospital, and Institute of Translational Medicine, Zhejiang University School of Medicine, Hangzhou, China; [7]Department of Orthopedic Surgery, Wuhan Union Hospital, Tongji Medical School, Huazhong University of Science and Technology, Wuhan, China; [8]Spine Service, Department of Orthopedic Surgery, St. George Hospital, Kogarah, NSW, Australia

Although cigarette smoking (CS) and low back pain (LBP) are common worldwide, their correlations and the mechanisms of action remain unclear. We have shown that excessive activation of mast cells (MCs) and their proteases play key roles in CS-associated diseases, like asthma, chronic obstructive pulmonary disease (COPD), blood coagulation, and lung cancer. Previous studies have also shown that MCs and their proteases induce degenerative musculoskeletal disease. By using a custom-designed smoke-exposure mouse system, we demonstrated that CS results in intervertebral disc (IVD) degeneration and release of MC-restricted tetramer tryptases (TTs) in the IVDs. TTs were found to regulate the expression of methyltransferase 14 (METTL14) at the epigenetic level by inducing N6-methyladenosine (m^{6}A) deposition in the 3′ untranslated region (UTR) of the transcript that encodes dishevelled-axin (DIX) domain-containing 1 (*DIXDC1*). That reaction increases the mRNA stability and expression of *Dixdc1*. DIXDC1 functionally interacts with disrupted in schizophrenia 1 (DISC1) to accelerate the degeneration and senescence of nucleus pulposus (NP) cells by activating a canonical Wnt pathway. Our study demonstrates the association between CS, MC-derived TTs, and LBP. These findings raise the possibility that METTL14-medicated DIXDC1 m^{6}A modification could serve as a potential therapeutic target to block the development of degeneration of the NP in LBP patients.

INTRODUCTION

Cigarette smoking (CS) is a global problem. Approximately 50% of young men and 10% of young women smoke worldwide. The World Health Organization (WHO) estimates that the global smoking population will increase to ∼1.6 billion by 2025.[1] Previous studies have shown that CS, but not alcohol consumption, is significantly correlated with low back pain (LBP).[2,3] A US survey of 9,282 adults showed that the prevalence of CS was 30% among those with LBP.[4] Some research reported that the desire to smoke is influenced by opioid pain medications and can be increased by the experience of LBP.[5]

Intervertebral disc degeneration (IVDD) is the most widely accepted reason for smoking and LBP. Some researchers have suggested that IVDD can be alleviated by cessation of smoking.[4] However, the detailed mechanisms by which CS promotes IVDD are unknown. We and others have demonstrated previously that excessive activation of mast cells (MCs) and the proteases they release play key roles in smoking-associated diseases, like asthma, chronic obstructive pulmonary disease (COPD), blood coagulation, and lung cancer.[6–11] It has been reported that immunoglobulin E (IgE)-dependent MC activation promotes the pathogenesis of osteoarthritis.[12] MCs and their prominent pro-inflammatory granule proteases mMCP-5/mCma1, mMCP-6/mTpsb2, and mMCP-7/mTpsab1 have prominent adverse roles in experimental arthritis, in part by indirectly destroying the aggrecan in cartilage.[13]

MCs are hematopoietic cells that complete their differentiation and maturation in tissues. Although MCs are preferentially located at

the portals of entry of pathogens (e.g., the tongue and skin), these effector cells of immune responses are present in nearly every organ. All human MCs store tetramer-forming tryptases in their secretory granules that are derived from the adjacent *hTPSAB1* and *hTPSB2* genes on human chromosome 16p13.3.[14] Hundreds of allelic variants of both genes have been identified by the Human Genome Project (some of which are not functional), but the major isoforms are so similar at the amino acid sequence level that this family of MC-restricted enzymes is collectively called tetramer tryptases (TTs). The corresponding TTs in mouse MCs are mouse MC protease (mMCP)-7/mTpsab1 and mMCP-6/mTpsab2. The MCs in the inbred BALB/c mouse strain express both proteases, but the inbred C57BL/6 mouse only expresses mMCP-6/mTpsb2 because of a slice-site mutation in the C57BL/6 mouse's mMCP-7/mTpsb2 gene.

Excessive activation of TT$^+$ MCs is thought to play key roles in bacterial infections and to prevent life-threatening internal blood clots but adverse roles in many inflammatory diseases (e.g., allergic inflammation, systemic mastocytosis, systemic anaphylaxis, asthma, arthritis, COPD, inflammatory bowel disease, and heart disease).[15] In our mouse model of CS-induced COPD, substantial pathology occurs in the lungs and other organs. For example, CS-exposed mice have fertility problems, colitis, and an enlarged heart. COPD is dependent on mMCP-6/mTpsb2 in this animal model.[7] Mouse and human MC TTs degrade the fibrinogen α chain, preventing internal blood clots.[8] These neutral proteases activate some matrix metalloprotease zymogens.[16] Although the relevant receptors on their responsive cells have not been identified, mouse and human TTs also induce endothelial cells, fibroblasts, and synoviocytes to increase their expression of numerous cytokines and other biologically active factors.

Exposure to environmental and lifestyle factors, particularly CS, has been demonstrated to significantly alter the epigenome, potentially leading to an increased risk of developing various diseases.[17] It is imperative to recognize the impact of epigenetic changes resulting from these factors and the potential health consequences they may entail. Of all internal mRNA modifications in mammalian cells, N6-methyladenosine (m^{6}A) is the most prevalent. m^{6}A participates in nearly every aspect of mRNA function and metabolism and in diverse cellular, developmental, and disease processes. Recent studies have highlighted the involvement of m^{6}A modification in the pathogenesis of disc degeneration.[18,19] Previous studies have explored the correlation between smoking and m^{6}A, with male smokers displaying lower peripheral blood RNA m^{6}A levels than non-smokers in a study of truck drivers.[20] Additionally, m^{6}A methylation has been shown to contribute to development of smoking-induced COPD and lung cancers.[21,22] Based on these findings, we hypothesize that smoking may act as a trigger for disc degeneration by regulating m6A methylation in the nucleus pulposus.

In this study, we describe a detailed mechanism by which MCs and their TT preformed mediators play a central role in CS-induced disc degeneration.

RESULTS

Exposure of mice to CS resulted in increased IVDD

To enable mechanistic studies, we examined the health of intervertebral discs (IVDs) in C57BL/6 mice who breathed room air or CS for 8 weeks and 12 weeks, as we reported previously.[6,7,9,11,23–27] These exposures are representative of a pack-a-day smoker.[28] Safranin O/fast green staining for the IVDs revealed that mice with 8 weeks of air exposure had healthy IVDs, characterized by aggrecan protein-rich, single-mass nucleus pulposus (NP) structure with normal cellularity and a clear-cut boundary between NP and annulus fibrosus (AF) tissues with intact concentric lamellar AF structures. On the other hand, the IVDs of mice that had been exposed to CS for 8 weeks showed degenerative phenotypes, including horizontal clefts inside the NP and the presence of non-vacuolated cells (Figure 1A, black box) and a serpentine lamellar structure in the AF (Figure 1A, yellow box)).

The level of degeneration became much more severe when comparing IVDs from 12-week CS-exposed mice with those from 12-week air-exposed mice. The NP of 12-week CS-exposed mice showed pronounced cell loss and non-vacuolated NP cells dispersed into the matrix (yellow box). The clear distinction between NP and AF tissue compartments was lost, and a cleft presented in AF layers (Figure 1B). We scored histological changes based on the modified Thompson scale (Table S1). The grade distributions for the NP and AF between air- and CS-exposed mice were significantly different at the 8-week and 12-week time points (Figures 1C and 1D). By using microcomputed tomography (micro-CT), we calculated the disc volume (VOL) and VOL per surface area. Interestingly, VOL and VOL/surface area were significantly decreased in 8-week CS-exposed spines at the L4/5 level instead of the L3/4 level (Figures 1E, 1F, S1A, and S1B). The spinal degeneration also includes morphology changes in vertebral bodies.[29] Parameters measured by micro-CT included bone volume (BV)/tissue volume (BV/TV) (Figure S1C), bone surface area (BSa)/BV (Figure S1D), trabecular thickness (Tb.Th) (Figure S1E), trabecular number (Tb.N) (Figure S1F), and trabecular spacing (Tb.Sp) (Figure S1G), which were used for assessing the microarchitecture of 8-week air- or CS-exposed mouse trabecular bones. The results indicated that CS exposed mice exhibited more trabecular BV in vertebral bodies than the respective air-exposed control mice, as demonstrated by significantly increased BV/TV and Tb.Th and significantly decreased BSa/BV in CS-exposed mouse vertebral bodies. However, the Tb.N and Tb.Sp showed no significant difference between the two groups.

Previous investigations have demonstrated that bone marrow-derived mesenchymal stem cells (BM-MSCs) could develop toward an NP-like phenotype *in vitro*.[30]

To study whether CS exposure could have effects on chondrogenesis capacity of BM-MSCs, mMSCs (mouse mesenchymal stem cells) were isolated from BM of mice exposed to 12 weeks of air or CS. After 2D osteogenesis and chondrogenic differentiation, BM-MSCs isolated
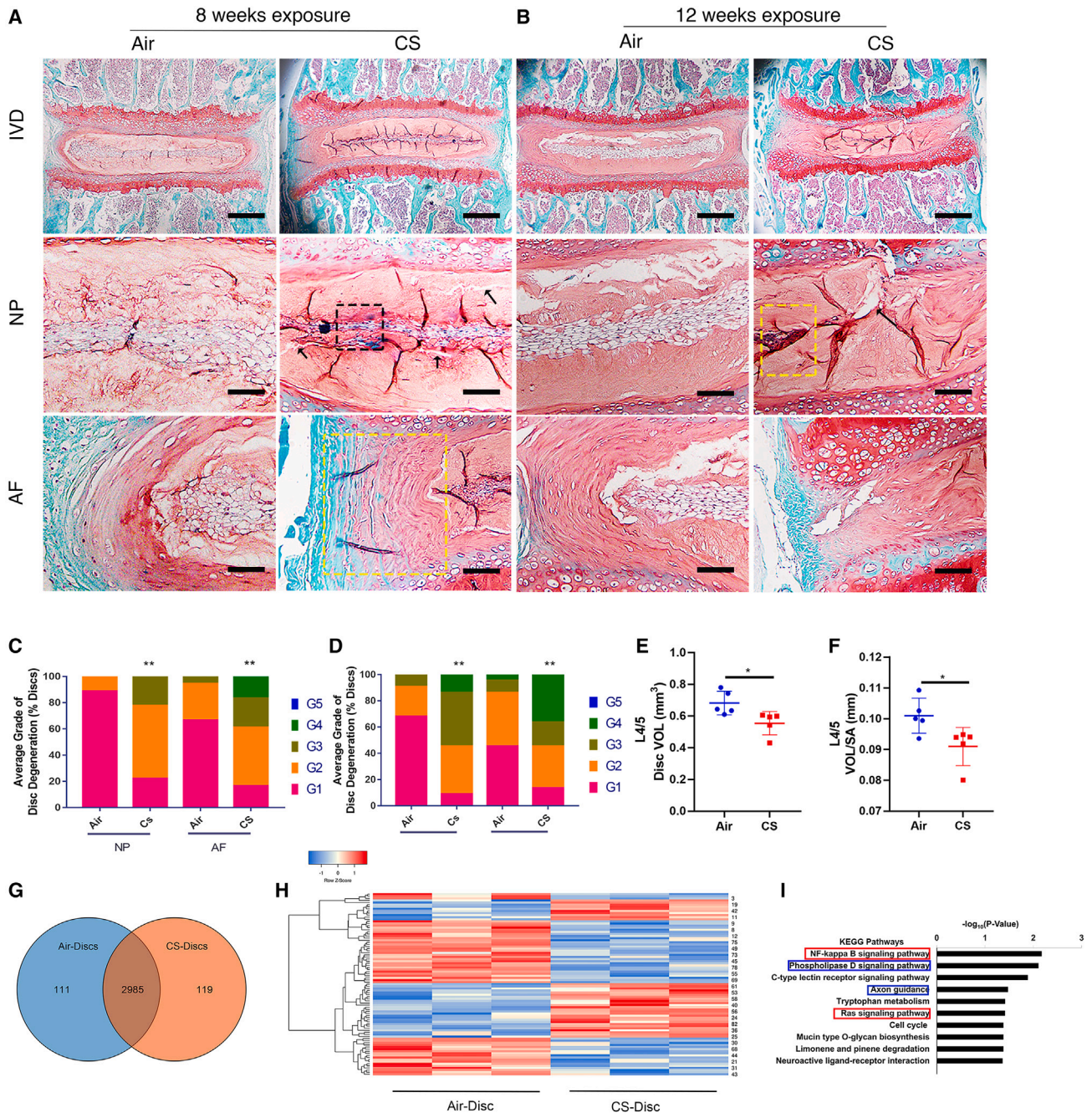
Figure 1. CS-exposed mouse IVDs showed accelerated structural degeneration

(A and B) Safranin O/fast green staining of coronal sections of IVDs from mice exposed to air or CS for 8 or 12 weeks (top row: scale bars, 200 μm; center row: scale bars, 50 μm; bottom row: scale bars, 50 μm). High-magnification views of NP and AF tissue are arranged below the IVD images for each group. (C and D) Histological grading using the modified Thompson scale, showing significant differences between air- and CS-exposed mice in the proportion of degenerated NP and AF at 8 and 12 weeks. Data were collected from 3 discs per mouse (n = 6 mice per group). Ridit analysis was performed. **p ≤ 0.01. (E and F) Micro-CT revealed changes in IVD structure between mice exposed to air or CS. Parameters included disc volume (VOL) and VOL/surface area at the L4/5 level after 8 weeks of air or CS exposure; n = 5 for each group, *p ≤ 0.05. Statistical analyses were performed with Student's t test. (G) Venn diagram showing the numbers of proteins identified from IVD samples (FDR < 0.01, unique peptides ≥ 2). The cross-section shows the number of common proteins between IVDs from air- and CS-exposed mice, while the two sides show the numbers of uniquely expressed proteins. (H) Heatmap showing the hierarchical clustering of differentially expressed proteins (DEPs; p < 0.05) between IVDs from air- and CS-exposed mice. Protein abundance is expressed using a standardized scale ranging from −2 to 2. High expression of a given pathway is marked with red, while low expression is marked with blue. White indicates intermediate expression. (I) KEGG analysis showing the top 10 enriched signaling pathways in IVDs from CS-exposed mice.
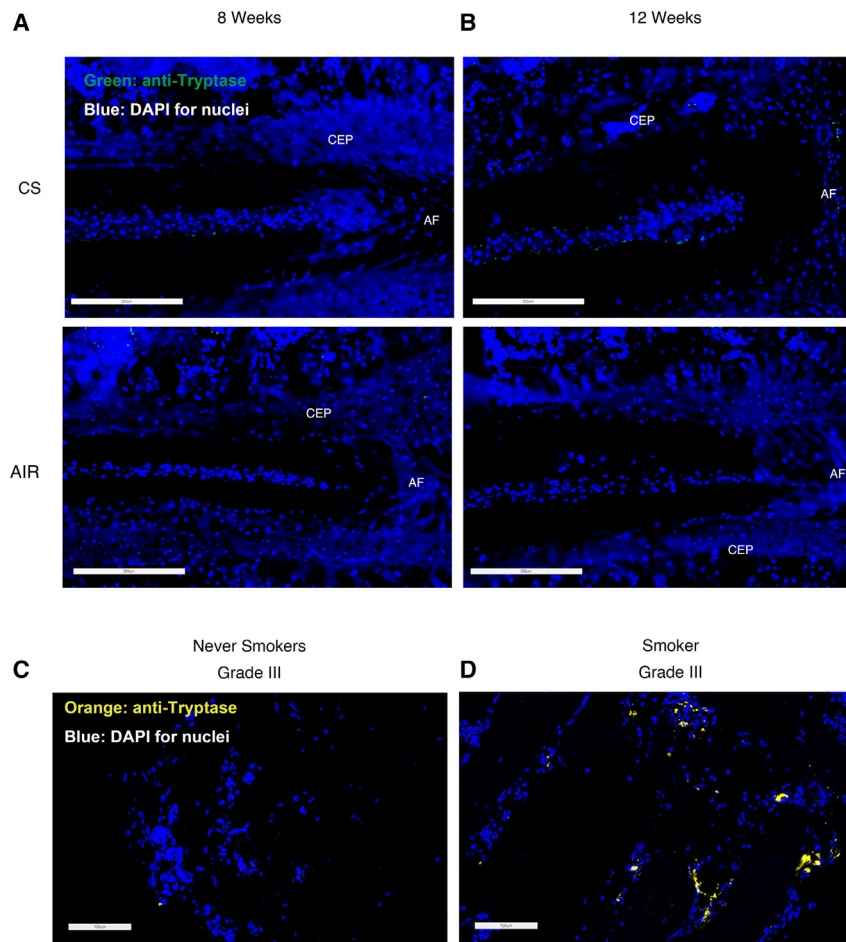
Figure 2. Elevated TT in the IVDs of CS-exposed mice and patients with IVDD who smoke

(A and B) IF staining for mMCP-6 in IVDs from mice exposed to air or CS for 8 weeks and 12 weeks. Levels of mMCP-6 are shown in green, and nuclei/DAPI are shown in blue. Scale bars, 200 μm. (C and D) The expression of tryptase is shown in orange, and nuclei/DAPI are shown in blue. Scale bars, 100 μm.

from air-exposed mice showed a stronger chondrogenesis capacity than cells isolated from CS-exposed mice (Figures S1H and S1I).

To further investigate the effects of CS on IVDs, label-free proteomics was conducted for IVDs from mice on 12 weeks of air and CS exposure. After MaxQuant searching, 3,096 and 3,084 proteins were identified from IVDs from air- and CS-exposed mice, respectively (Figure 1G). A list of these proteins is shown in Table S2. The heatmap across differentially expressed proteins (DEPs; false discovery rate [FDR]-adjusted p < 0.05) shows that most proteins enriched in IVDs were from air- and CS-exposed mice (Figure 1H). To increase the confidence in the pathway analysis and correct for multiple testing, only DEPs with a log2 fold change equal to or greater than 1 and equal to or less than −1 were identified. The DEPs are shown in Table S3.

The top 10 enriched signal pathways in IVDs from 12-week CS-exposed mice were analyzed by using Kyoto Encyclopedia of Genes and Genomes (KEGG) analysis. Notably, two vital pathways, which are IVD degeneration related, including nuclear factor κB (NF-κB) signaling pathways[31] and the Ras signaling pathway,[32] were enriched

(Figure 1I, red box). The phospholipase D signaling pathway[33] and axon guidance pathway,[34] which are play key roles in pain sensitivity, were enriched (Figure 1I, blue box).

We also used the Protein Annotation Through Evolutionary Relationships (PANTHER) database[35] to classify the list of DEPs into categories according to biological process, molecular function, and cellular component. Based on ontology terms, the DEPs were found to be associated with regulation of multicellular organismal processes (18.18%), response to drug (9.09%), and regeneration (3.5%) (Figure S2A). For molecular functions, the DEPs were classified into 15 subgroups. The most abundant subgroups were protein dimerization activity (12.73%), peptidase activity (8.18%), and oxidoreductase activity (3.64%) (Figure S2B). Following categorization by cellular component, proteins were mostly grouped into other unclassified cellular components (77.04%); for other components, the most abundant subgroups were striated muscle thin filament (3.45%) and organellar ribosome (2.3%) (Figure S2C). A list of significantly different potential protein networks was predicted in the IVDs of CS-exposed mice compared with air-exposed mice (Figure S2D).

Elevated TTs in the IVDs of CS-exposed mice as well as patients with IVDD who smoke

It has been suggested that a minority of human herniated discs possess MCs.[36] Guided by the knowledge that MCs are key contributors to the pathophysiological inflammatory processes that underpin smoking-related diseases, including asthma and COPD, as we and others have shown previously, we hypothesized that MCs may play a role in CS-induced IVDD.[6–11,37,38] We analyzed IVD tissues from air- and CS-exposed mice for the MC TT mMCP-6. The results showed that there is increased expression of mMCP-6 in the NP region of IVDs from 8- and 12-week CS-exposed mice (Figures 2A, 2B, and S3A). We then analyzed the expression of TTs in NPs from smokers and never smokers. To mimic the bias from the degree of IVDD, grade III IVDs were selected for smokers and never smokers. The results showed that expression of human TT (hTT) is elevated in NP tissues from smokers compared with those from never smokers (Figures 2C, 2D, and S3B). The serum IgE levels, one of the MC
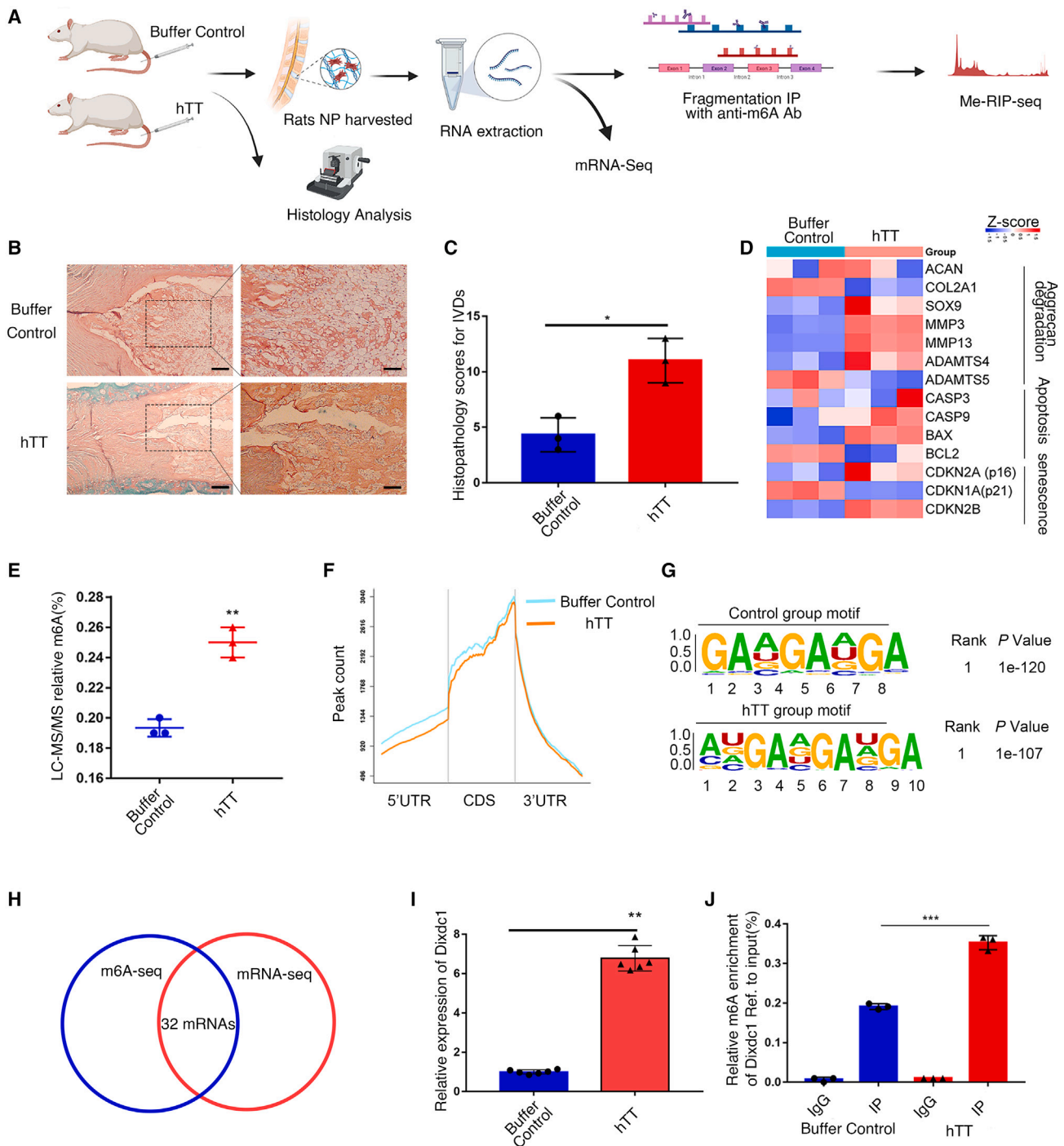
Figure 3. hTT induces NP degeneration and mRNA methylation of the NP *in vivo*

(A) Graphical representation of the experimental workflow. (B) Representative image of safranin O/fast green staining of hTT/control-injected IVDs. (C) Histological grading scale for safranin O/fast green staining. (D) Heatmap showing mRNA expression for genes related to IVD degeneration in NPs from hTT/control-injected IVDs. (E) LC/MS-MS assay was used to measure the m[6]A level for mRNA of NPs from hTT/control-injected IVDs. Data are shown as the mean ± SD, n = 3. **p < 0.01, two-tailed unpaired Student's t test. (F) Distribution of m[6]A peaks across the start codon, CDS, and stop codon of mRNA transcripts. The moving averages of NPs from hTT-injected IVDs (red)

(legend continued on next page)

stimuli, were found to be significantly elevated in patients who are smokers compared with never smokers (Figure S3C).

hTT induces NP degeneration and mRNA methylation of the NP *in vivo*

The rat IVDD model was built as reported previously.[39] Discs were harvested at week 4 after single injection and evaluated using histology. The NP was isolated from rat IVDs for bulk RNA sequencing (RNA-seq) and methylation RNA immunoprecipitation sequencing (MeRIP-seq) (Figure 3A). The IVD specimens from the control/hTT injection groups were subjected to Safranin O/fast green stain. We evaluated the histology results based on a standardized histopathology scoring system for IVD degeneration in rat models.[40] The NPs from control-injected groups showed a rounded/oval shape with mild distortion and slightly decreased of NP cell (NPC) numbers (>2/3 of NP space). The AF was well organized. In hTT-treated groups, the NPC number were significantly decreased, the boundary of NP and AF was lost, and the AF was disorganized (Figure 3B). Overall, we scored the rats' IVD histology, and statistical results showed that hTT injection induced significant severe degeneration compared with control injection (Figure 3C).

RNA-seq showed that catabolic mRNA, such as mixed-member proportional representation (MMP)-3 and -13, and a disintegrin and metalloprotease with thrombospondin type I motifs 4 (ADAMTS-4) were elevated in hTT-injected groups. Apoptosis mRNA, such as caspase-9 (CASP 9) and BCL2-associated X (Bax)/BCL2 apoptosis regulator (Bcl-2) ratio, and cell senescence mRNA, such as cyclin-dependent kinase inhibitor 2A (CDKN2A) and CDKN2B, were elevated in hTT-injected groups as well (Figure 3D). A list of differentiated expressed mRNAs can be found in Table S4.

m^6A is the most abundant mRNA internal modification and has been reported to play critical roles in gene expression in diverse physiological and pathological processes.[41] Previous studies have shown that mutation of methyltransferase 3 (METTL3), an m^6A writer protein, leads to disc degeneration in needle puncture rat models.[18] Fat mass- and obesity-associated protein (FTO) and lncRNA-regulated GSK3β/Wnt have been shown to play a crucial role in disc degeneration in rat models.[42] These findings provide a foundation for investigation of the role of m^6A in disc degeneration and support our focus on this modification in our current study. By using liquid chromatography-tandem mass spectrometry (LC-MS/MS), we identified that the m^6A levels in NPs of hTT-injected IVDs were statistically more abundant than in control-injected NPs (Figure 3E). By employing m^6A-seq, we identified a total of 11,257 distinct peaks in the RNAs of 6,082 genes in control groups and a total of 11,203 distinct peaks in the RNAs of 6,136 genes in hTT groups. Of these peaks, most of them resided in in-

trons and coding sequences (CDSs), and a few unique peaks were mapped to the 5′ UTR and 3′ UTR (Figures 3F, S4A, and S4B). The m^6A consensus motif of GGAGA was presented in both mRNAs of NP tissues from control and hTT-injected IVDs (Figure 3G).

DIX domain-containing 1 (*Dixdc1*) is identified as the hTT downstream target during degeneration

MeRIP-seq showed that the m^6A peaks of 260 transcripts exhibited a significant difference between hTT-treated and control groups (fold change of at least 1.5, p < 0.05; Table S5). After integrating the mRNA-seq and m^6A sequencing (m^6A-seq) results, we found that 32 differentiated expressed mRNAs were m6A-regulated genes (Figure 3H). Among these genes, *Dixdc1* was considered a potential disc degeneration-related target given that it is correlated with IVD degeneration severity based on our previous single-cell RNA analysis (GSE165722) and its characteristic of being a positive regulator of the *Wnt* signaling pathway, an important catabolic pathway in IVD degeneration.[43–46] We further determined the mRNA expression of *Dixdc1* by quantitative real-time PCR (qRT-PCR) in both groups; the results indicated *Dixdc1* to be significantly elevated in the RNA of NPs from hTT-injected IVDs (Figure 3I). Then MeRIP-qPCR assays with specific primers aiming at potential m^6A sites revealed that hTT injection could significantly promote m^6A modification of *Dixdc1* in the 3′ UTR (Figure 3J).

hTT induces human NPC (hNPC) degeneration and mRNA methylation by removing the repressive mark H3K9me3 at the METTL14 promoter

Because the hTT effects on NP were explored *in vivo*, we next analyzed its effects on hNPCs. We isolated hNPCs from patients who underwent microdiscectomy (Figure 4A), treated them with control/hTT, and performed mRNA-seq. KEGG analysis showed that degeneration pathways, such as the hippo signaling pathways and cellular senescence, were enriched in hTT-treated hNPCs (Figure 4B). Because the cell cycle pathways were enriched in hTT-treated hNPCs, we determined whether hTT-treated hNPCs express a broad cell-cycle-associated transcriptional program or only select genes. When analyzed select genes associated with specific cell cycle phases that revealed differential expression patterns between two groups, we found hTT-treated hNPCs predominantly expressing markers of quiescence or stalling in G1. Moreover, most S phase-associated transcripts were found to be highly expressed in hTT-treated hNPCs. In contrast, untreated hNPCs expressed lower levels of quiescence or early G1 markers but high expression of G1/S phase markers and G2-specific and M phase transcripts (Figure S4C).

SDS-PAGE immunoblot results showed that expression of anabolic proteins, aggrecan (*ACAN*) and collagen II, was decreased, while

---

and that from buffer control-injected IVDs peak percentage (blue) are shown. (G) Top consensus motif identified DREME with m^6A-seq in NPs from hTT/control injected IVDs. (H) A Venn diagram was generated from the gene sets enriched for transcripts that were substantially altered for mRNA-seq along with those enriched for m^6A-modified transcripts (m^6A-seq). (I) The mRNA level of DIXDC1 in NPs from hTT/control-injected IVDs. Data are shown as the mean ± SD, n = 3. **p < 0.01, two-tailed unpaired Student's t test. (J) m^6A modification of DIXDC1 was detected by MeRIP-qPCR analysis using anti-IgG and anti-m^6A Abs. Relative m^6A enrichment of DIXDC1 mRNA for each IP group was normalized to input. Data are shown as the mean ± SD, n = 3. ***p < 0.001, two-tailed unpaired Student's t test.
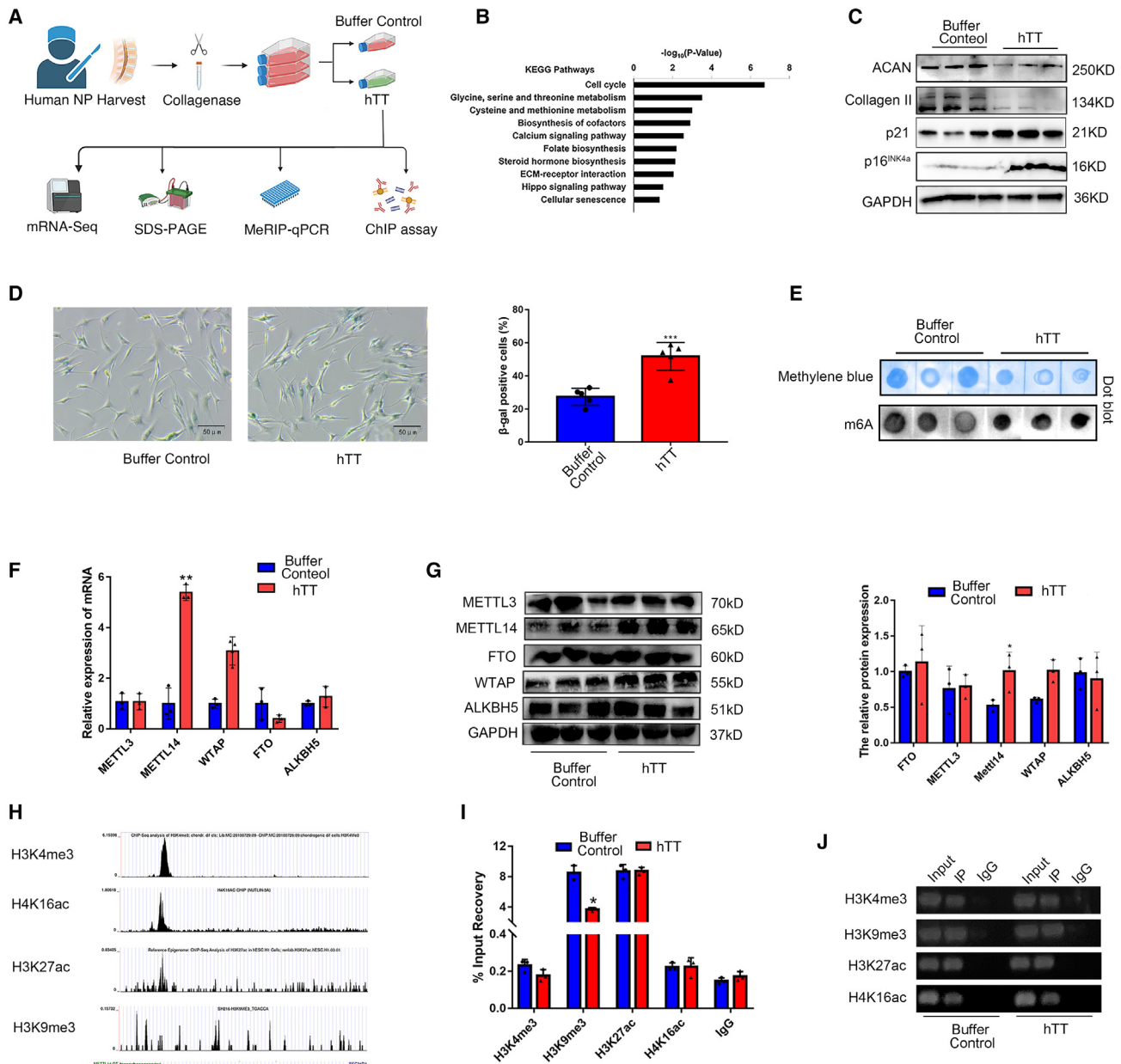
Figure 4. hTT induced human NPC degeneration and mRNA methylation by removing the repressive mark H3K9me3 at the *METTL14* promoter

(A) Graphical representation of the hNPC experimental workflow. (B) Top 10 significantly enriched KEGG pathways of hTT-treated hNPCs. (C) Expression of the anabolic proteins *ACAN* and *collagen II* and the cell senescence proteins *p21* and *p16^INK4a* in hNPCs treated with hTT and buffer control. (D) Representative image and quantification of SA-β-gal staining in hNPCs treated with hTT and buffer control. Data are shown as the mean ± SD, n = 5. **$p < 0.01$, two-tailed unpaired Student's t test. (E) The m6A level alterations after hTT treatment were measured by m6A RNA dot blot assay. (F) The mRNA levels of m6A readers and writers in hTT-treated hNPCs were measured using qRT-PCR. Data are shown as the mean ± SD, n = 3. **$p < 0.01$, two-tailed unpaired Student's t test. (G) The protein levels of m6A readers and writers in hTT treated hNPCs were measured using SDS-PAGE immunoblotting. Right: quantification of SDS-PAGE immunoblot results from (G). (H) Snapshots of the UCSC genome browser, showing METTL14-binding histone epigenetic modification events at its promoters. (I and J) Enrichment for H3K4me3, H4K16ac, H3K27ac, and H3K9me3 modifications was assessed by ChIP qPCR on METTL14. Data are shown as the mean ± SD, n = 3. *$p < 0.05$, two-tailed unpaired Student's t test.

cell senescence proteins, p21 and p16^INK4a, were elevated upon hTT treatment (Figure 4C). The number of cells with senescence-associated β-galactosidase (SA-β-gal) staining, a classic indicator of senescence, were increased with hTT treatment (Figure 4D). These results indicated that hTT induced degeneration and cell senescence in hNPCs.

We applied dot blot assays and found that hTT treatment led to increased m[6]A levels in hNPCs (Figure 4E). We further assessed the expression of the most important m[6]A regulatory factors: methylases (including *METTL3*, *METTL14*, and WT1-associated protein [*WTAP*]) and demethylases (*FTO* and human AlkB homolog H5 [*ALKBH5*]). Notably, qRT-PCR revealed that *METTL14* and *WTAP* were upregulated in hTT-treated NPCs compared with control NPCs (Figure 4F). SDS-PAGE immunoblotting showed that only METTL14 levels were significantly higher in hTT-treated NPCs compared with control NPCs (Figure 4G). These results indicated that METTL14 might be a major m[6]A-regulating factor, accounting for the high level of m[6]A modification in hTT-treated hNPCs.

Chromatin modification, especially histone modification, is the fundamental mechanism in a myriad of cellular and developmental processes.[47] Previous studies indicated that histone modifications can determine specific and dynamic deposition of m[6]A in mRNA.[48] To verify whether hTT-induced elevated expression of METTL14 could be regulated by histone epigenetic modification, we used the online tools Cistrome Data Browser[49] and UCSC Genome[50] to predict and visualize four kinds of histone modifications of *METTL14* mRNA, including Trimethylation of Histone H3 at Lysine 4 (H3K4me3), Histone H4 acethylation at Lysine 16 (H4K16ac), Histone 3 lysine 27 acetylation (H3K27ac), and Histone 3 lysine 9 trimethylation (H3K9me3). The chromatin immunoprecipitation sequencing (ChIP-seq) database showed enriched profiles for four histone modification across the transcription start sites (TSSs) of *METTL14* (Figure 4H). In addition, the ChIP-seq data were validated by ChIP-qPCR tests on hTT- and control-treated hNPCs. The results indicated that, although these four-histone modifications were distributed in the TSS region of *METTL14*, only the level of H3K9me3 showed a significant difference between two groups. The levels of H3K9me3 at *METTL14* TSS regions were significantly decreased in hTT-treated hNPCs compared with control-treated hNPCs (Figures 4I and 4J).

hTT induced hNPCs degeneration via METTL14-mediated *DIXDC1* upregulation

Because we identified *DIXDC1* as the candidate target of hTT in our rat models (Figure 3H), we examined the results in hNPCs. qRT-PCR showed that expression of *DIXDC1* was elevated upon hTT treatment (Figure 5A). The MeRIP-qPCR results indicated that hTT could significantly promote m6A modification of *DIXDC1* in 3′ UTR in hNPCs (Figure 5B). To further explore the role of METTL14 in *DIXDC1* expression, short hairpin RNAs (shRNAs) that target transcripts of *METTL14* were employed in this study (Figure S5A). We applied dot blot assays, and the m[6]A level was increased in hTT-treated hNPCs but decreased with *METTL14* knockdown (Figure 5C). Inhibition of *METTL14* significantly impaired the increased *DIXDC1* expression in hTT-treated hNPCs (Figure 5D). The stability of *DIXDC1* was evaluated in METTL14 knockdown cells. The results demonstrated that *METTL14* knockdown can decrease *DIXDC1* stability in hNPCs (Figure 5E).

To further assess the biological role of *METTL14* and *DIXDC1* in hNPC degeneration, we overexpressed *DIXDC1* or *METTL14* in hNPCs by plasmids. Our analysis indicated that *METTL14* or *DIXDC1* overexpression decreases the expression of the anabolic markers ACAN and collagen II. Expression of the cell senescence markers p21 and p16[INK4a] significantly increased when METTL14 or *DIXDC1* was overexpressed (Figure 5F). To assess the effect of *METTL14* or *DIXDC1* inhibition on hTT-induced hNPC degeneration, shRNAs that target transcripts of *METTL14* or *DIXDC1* were employed in hTT-treated hNPCs (Figure S5B). As depicted in Figure 5G, we observed that hTT significantly decreased the expression of ACAN and collagen II but significantly increased the expression of p21 and p16[INK4a]. Moreover, *DIXDC1* or *METTL14* knockdown, combined with hTT treatment, caused increased expression of ACAN and SOX9 but decreased expression of p21 and p[16INK4a] (Figure 5G). SA-β-gal staining showed significantly decreased senescence cells with knockdown of METTL14 in hTT-treated hNPCs (Figure 5H). Because we found that *METTL14* and *DIXDC1* are elevated in hTT-treated hNPCs, we explored expression of these two proteins in air- or CS-exposed mouse IVDs. The results indicated that expression of METTL14 and DIXDC1 was elevated in NP tissue in CS-exposed mice at the 8-week and 12-week time points (Figures S5C and S5D).

Biochemical characterization of the interaction between the 3′ UTR of *DIXDC1* and METTL14 protein

We conducted RNA immunoprecipitation (RIP) assay using METTL14 antibody to analyze the interaction between the 3′ UTR of *DIXDC1* and *METTL14* in hTT-treated hNPCs. The results show high binding activity of METTL14 and the 3′ UTR of *DIXDC1* mRNA, implying that *DIXDC1* may be regulated at the RNA level upon interaction with METTL14 (Figure 6A). Combined fluorescence *in situ* hybridization (FISH) using a *DIXDC1* 3′ UTR probe and immunofluorescence with METTL14 Abs were performed for hNPCs transfected with empty plasmid DNAs (pcDNA) or a plasmid encoding *DIXDC1*(*DIXDC1* overexpression [OE]). The results indicated co-localization of the *DIXDC1* 3′ UTR and METTL14 protein. However, OE of the *DIXDC1* coding region does not impact the co-localization ratio (Figure S5E).

We applied sequence-based RNA adenosine methylation site predictor (SRAMP)[51] to predict the m[6]A sites of the 3′ UTR of *DIXDC1*. The results indicated a GAACU motif located at 68 bp, which is predicted to be a high-confidence m[6]A site in all predicted sites (Table S6). Then we used the Rosetta software package[52,53] and Alphafold[54] to predict and analyzed the METTL14 protein structure. We also predicted the RNA structure of the 3′ UTR of *DIXDC1* by using RNAfold.[55] Then the interaction of METTL14 protein and the 3′ UTR of *DIXDC1* was analyzed. A domain region located at the 245–296 amnio acids of METTL14 was identified as the most possible interaction site with the GAACU motif on the 3′ UTR of *DIXDC1* (Figure 6C). Taken together, these results demonstrate that METTL14 directly interacts with the 3′ UTR of *DIXDC1*.
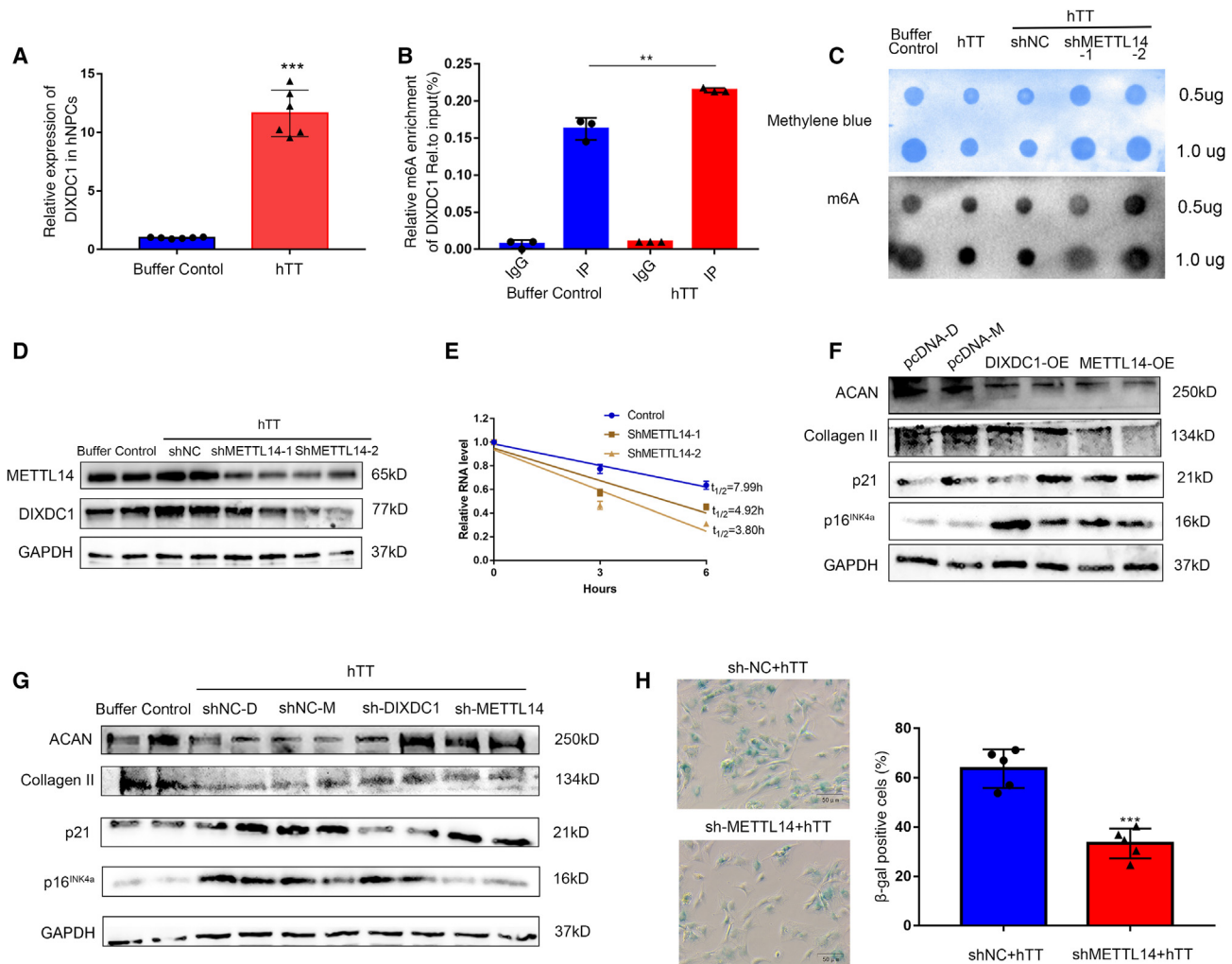
Figure 5. hTT induced hNPCs degeneration via METTL14-mediated *DIXDC1* upregulation

(A)The mRNA levels of DIXDC1 in hTT-treated hNPCs were measured using qRT-PCR. Data are shown as the mean ± SD, n = 6. ***p < 0.001, two-tailed unpaired Student's t test. (B) MeRIP qRT-PCR was used to detect m^{6}A level alterations of DIXDC1 after hTT treatment in hNPCs. Data are shown as the mean ± SD, n = 3. **p < 0.005, two-tailed unpaired Student's t test. (C) The m6A content of total RNAs in buffer control-treated, hTT-treated, shNC, and METTL14 knockdown hNPCs (left panel) was detected using a dot blot with an m6A Ab. Methylene blue staining served as the loading control (right panel). (D) The protein levels of METTL14 and DIXDC1 in hTT-treated hNPCs with or without METTL14 knockdown were measured using SDS-PAGE immunoblot. (E) Lifespan of DIXDC1 expression in hTT-treated hNPCs transfected with the reduction of METTL3. Relative mRNA levels were quantified by qRT-PCR. Data are shown as the mean ± SD, n = 6. (F) Expression of the anabolic proteins ACAN, collagen II, and SOX9 and the cell senescence proteins p21 and p16^{INK4a} in hNPCs treated with DIXDC1 or METTL14 OE. (F) Expression of the anabolic proteins ACAN and collagen II and the cell senescence proteins p21 and p16^{INK4a} in hNPCs treated with DIXDC1 or METTL14 OE. (G) Expression of the anabolic proteins ACAN and collagen II and the cell senescence proteins p21 and p16^{INK4a} in hNPCs treated with hTT with or without DIXDC1 or METTL14 knockdown. (H) Representative image and quantification of SA-β-gal staining in hNPCs treated with hTT or hTT + METTL14 knockdown. Data are shown as the mean ± SD, n = 5. ***p < 0.001, two-tailed unpaired Student's t test.

hTT enhanced the mRNA stability of *DIXDC1* via IGF2BP1

Because we proved that METTL14 knockdown could decrease the stability of *DIXDC1* mRNA (Figure 5E), we next investigated potential effects of "reader" proteins in the process illustrated above. Upon m6A methylated mRNA export to the cytoplasm, it binds to specific cytosolic "reader" proteins, which can affect mRNA stability.[41,56] The YTHDF family (YTHDF1/2/3) mRNA-binding proteins 1, 2, and 3 (IGF2BP1/2/3) are mostly well analyzed for RNA stability regulation.[56,57]

The SDS-PAGE immunoblot results showed that expression of YTHDF1/2/3 and IGF2BP1/2 was elevated upon hTT treatment (Figure 7A). To identify the reader that recognizes the 3′ UTR of *DIXDC1*, an RNA pull-down assay was performed. The results indicated that IGF2BP1 and IGF2BP2 interacted with the 3′ UTR of *DIXDC1* (Figure 7B). To explored the effects of IGF2BP1 and 2 on *DIXDC1* expression, we next knocked down IGF2BP1 and IGF2BP2 using two specific small interfering RNAs (siRNAs) and explored expression of *DIXDC1* (Figures S5F and S5G). The
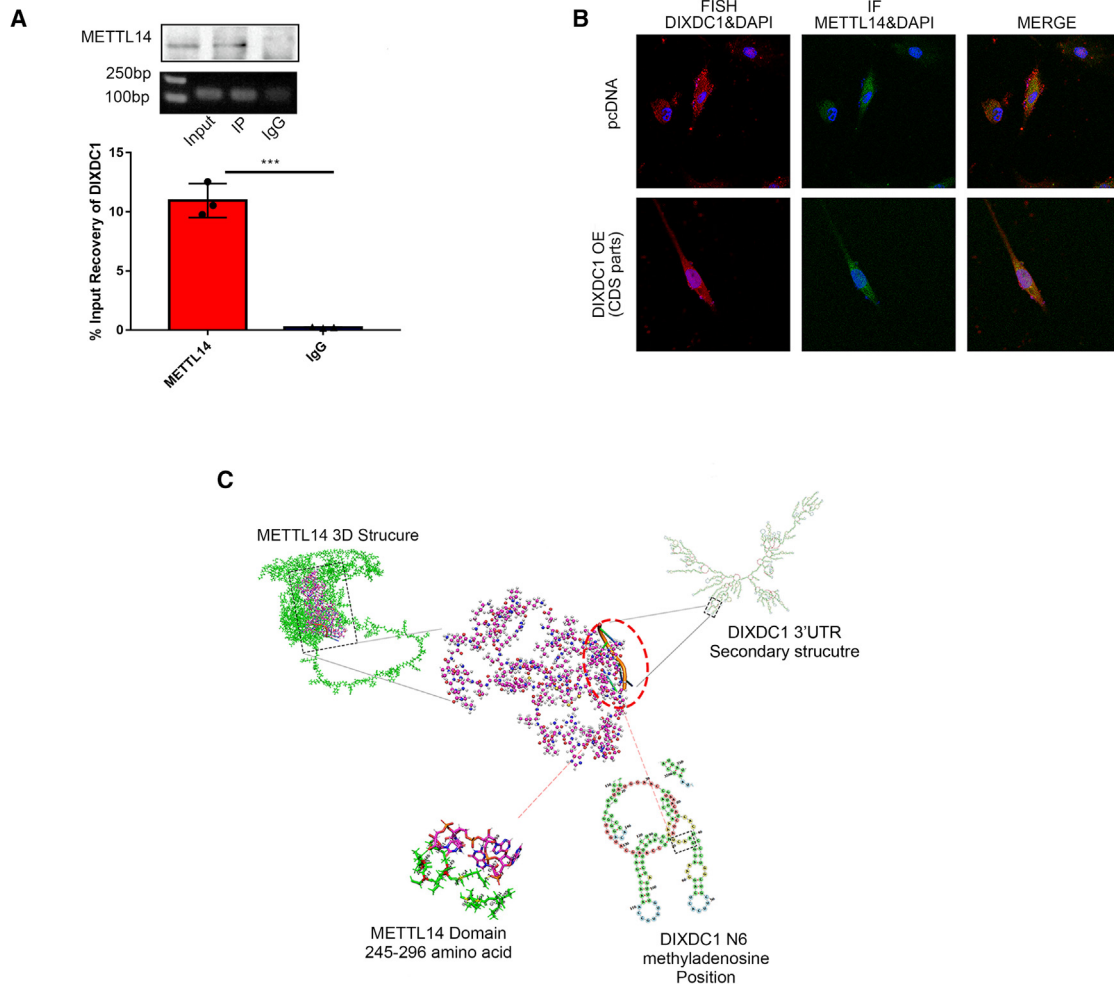
Figure 6. Biochemical characterization of interaction between *DIXDC1* and METTL14 protein

(A) RIP assays for METTL14 were performed, and the coprecipitated RNA was subjected to qRT-PCR for DIXDC1 (top panel). Agarose electrophoresis of PCR products is shown on the right. Experiments were performed in triplicate, and data are presented as mean ± SD. ***p < 0.001. (B) hNPCs were transfected with pcDNA-DIXDC1. The colocalization of METTL14 and DIXDC1 mRNA in hNPCs was examined by *in situ* hybridization using a fluorescently labeled DIXDC1 mRNA-specific probe, followed by immunocytochemistry with anti-METTL14 Abs and nuclei stained with DAPI. The distribution of DIXDC1 mRNA is shown in red, and METTL14 is shown in green. (C) Visualization of the interaction between the 3D structure of METTL14 (calculated by Rosetta) and the secondary structure of the 3′ UTR of DIXDC1 (calculated by Alphafold).

results showed that only IGF2BP1 knockdown can abolish the increased expression of *DIXDC1* induced by hTT treatment (Figure 7C). The stability of *DIXDC1* was evaluated in IGF2BP1 knockdown cells. The results demonstrated that IGF2BP1 knockdown can decrease *DIXDC1* stability in hTT-treated hNPCs (Figure 7D).

DIXDC1 activates the canonical but not the noncanonical Wnt pathway

DIXDC1 has been identified as a positive regulator of *Wnt* signaling in zebrafish.[58] We utilized a luciferase reporter construct containing eight copies of the TCF/LEF binding site (8XSuperTOPFLASH) to measure Wnt-mediated GSK3b/β-catenin activity. The results showed that knockdown of *DIXDC1* expression could significantly

reduce *Wnt3a*-stimulated TCF/LEF reporter activity compared with shRNA controls (Figure 7E). Moreover, the Wnt pathway inhibitor SM04690 attenuated matrix degradation and cell senescence induced by *DIXDC1* OE (Figure 7F).

Previous literature shows that DIXDC1 plays its role through interaction with other proteins, like disrupted in schizophrenia 1 (DISC1).[59] We explored whether DIXDC1 can interact with DISC1 in hNPCs. We found that DIXDC1 and DISC1 coimmunoprecipitated in hNPCs, demonstrating that they form a complex in hNPCs (Figure 7G). However, DIXDC1 does not coimmunoprecipitate with Ca^{2+}/calmodulin-dependent protein kinase II (CaMKII), an important noncanonical Wnt signaling pathway protein. Although expression of CaMKII was increased upon
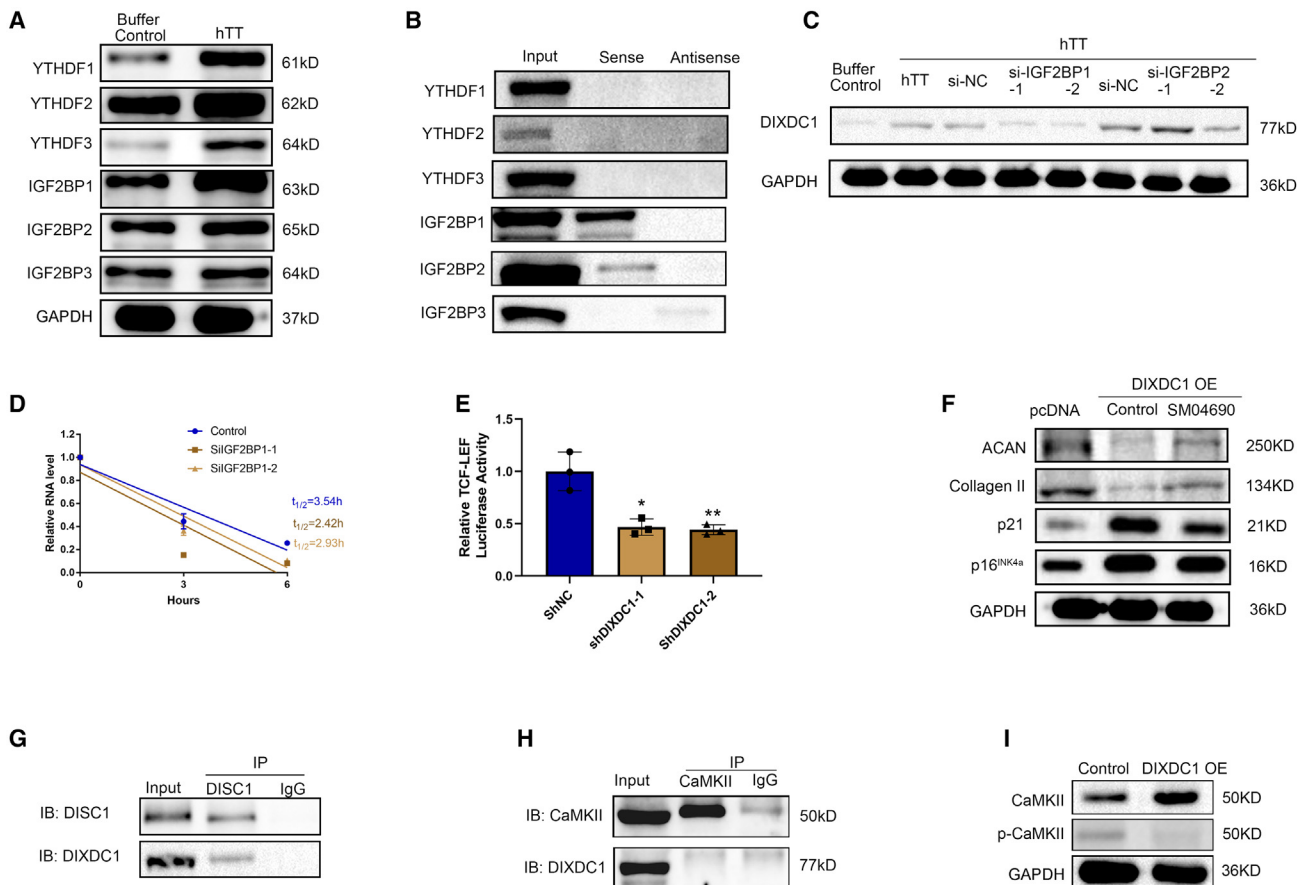
Figure 7. hTT enhances the stability and half-life of *DIXDC1* mRNA via IGF2BP1 and activation of the Wnt pathway

(A)The protein levels of "readers" in hTT- or control-treated hNPCs were measured using SDS-PAGE immunoblot; GAPDH was used as the loading control. (B) RNA pull-down assays and SDS-PAGE immunoblot showed that IGF2BP1 and IGF2BP2 could bind the 3′ UTR of DIXDC1 in hNPCs. (C) The expression of DIXDC1 in hNPCs with knockdown of IGF2BP1or IGF2BP2 combined with hTT treatment using SDS-PAGE immunoblot. GAPDH was used as the loading control. (D) Lifespan of DIXDC1 expression in hTT-treated hNPCs transfected with the reduction of IGF2BP1. Relative mRNA levels were quantified by qRT-PCR. Data are shown as the mean ± SD, n = 6. (E) hNPCs cells were transfected with the TOPFLASH reporter and control or Dixdc1 shRNA, followed by stimulation with Wnt3a conditioned medium, and subjected to a luciferase assay. The graph shows the relative TCF/LEF luciferase activity. Data are shown as the mean ± SD, n = 3. *p < 0.05, **p < 0.01, two-tailed unpaired Student's t test. (F) Expression of the anabolic proteins ACAN and collagen II and the cell senescence proteins p21 and p16^{INK4a} in hNPCs treated with control plasmid, DIXDC1 OE, or DIXDC1 OE plus SM04690 using SDS-PAGE immunoblot; GAPDH was used as the loading control. (G) The endogenous interaction between DISC1 and DIXDC1 was detected using coimmunoprecipation. Then, the anti-DISC1 or anti-Dixdc1 immunoprecipitants were immunoblotted with anti-DISC1 or Dixdc1 Abs, respectively. (H) The endogenous interaction between CaMKII and DIXDC1 was detected using coimmunoprecipation. Then, the anti-CaMKII or anti-Dixdc1 immunoprecipitants were immunoblotted with anti-CaMKII or Dixdc1 Abs, respectively. (I) The expression of CaMKII and p-CaMK II in hNPCs treated with control plasmid or DIXDC1 OE using SDS-PAGE immunoblot; GAPDH was used as the loading control.

DIXDC1 OE, phosphorylation of CaMKII was decreased after *DIXDC1* OE (Figures 7H and 7I). These results indicate that DIXDC1 activates the canonical Wnt Pathway, which might be correlated with the interaction with DISC.

DISCUSSION

MCs are relatively rare cells in disc tissues; however, they have potent activity of inducing inflammatory status. The recombinant mMCP-6/ TT has been shown to be the most potent inducer of selective and rapid accumulation of long-lasting neutrophils at injection sites.[60,61] The long-lasting effect of mouse and hTTs is due to their ability to induce bystander cells in the peritoneal cavity, lungs, and other tissues to selectively increase their expression of the interleukin-8 (IL-8) family of chemokines in a persistent manner.[61] The TT could also induce activation of macrophages in tissues.[7,13] MCPs can degrade the extracellular matrix by activating collagenolytic MMPs and urokinase-type plasminogen activator (uPA) involved in fibrosis. Human skin chymotrypsin-like proteinases (tryptase, chymase) can degrade normal human skin and lead to extensive epidermal-dermal separation.[62] Tryptase can activate MMP-3 or stromelysin in a time- and dose-dependent manner. When depleted of pro-MMP-3 by immunoadsorption, tryptase loses its capacity to generate active collagenase

in cultured rheumatoid synoviocytes.[63] Tryptase is also a potent activator of single chain (sc) uPA (or pro-urokinase), the zymogen form of uPA. In contrast, some studies have reported that tryptase can stimulate fibroblast proliferation and collagen synthesis. When normal dermis-derived fibroblasts were stimulated with human lung-derived tryptase, proliferation and production of type I collagen were increased significantly.[64] Chymase activates pro-collagenase in tissue by cleaving the Leu82-Thr83 bond without forming intermediate species.[65] Increased collagen synthesis by fibroblasts induced by tryptase can explain the mechanisms for abnormal fibrosis in inflammatory disorders.[66] Chymase releases latent transforming growth factor β1 from cultured leukocytes that can promote fibrosis.[67,68]

This study explored the detailed mechanisms of how hTT is involved in disc degeneration, and NPCs were explored in a rat model as well as in humans. DIXDC1 is a member of DIX domain-containing protein and is strongly linked to the Wnt signaling pathway, especially in neural development. In zebrafish, Ccd1, a homolog of human DIXDC1, was also found to be a positive regulator of the Wnt signaling pathway. It was suggested that DIXDC1 protein serves as an inhibitor of Dvl- and axin-mediated activation of the c-Jun N-terminal kinase pathway.[69] The DIXDC1 protein can be regulated by the Wnt/β-catenin pathway, and ubiquitin-dependent degradation of ectopic and endogenous DIXDC1 protein can be decreased by activation of canonical Wnt signaling.[70] Singh et al.[59] reported that DISC1 is regulated through interactions with DIXDC1 during embryonic neural progenitor proliferation and neuronal migration and that interactions can be modulated by Wnt-GSK3β/β-catenin signaling.[59] Expression of DIXDC1 is downregulated in human cancers, correlating with poor survival.[71] Mice lacking DIXDC1 have abnormal anxiety, depression, and social behavior.[44] Our single-cell RNA-seq data showed that DIXDC1 is upregulated in severe compared to mildly degenerated tissues. Thus, tryptase could induce IVD degeneration through upregulation of DIXDC1.

We showed an increase in trabecular bone (increased in BV/TV and Tb.Th) in CS-exposed mice by micro-CT; these results are consistent with a previous study.[72] Female B6 mice exhibited more trabecular BV in vertebral bodies following CS exposure for 4 weeks than air-exposed control mice.[72] Another study reported that no significant loss in vertebral trabecular BV was observed after 12 weeks of CS exposure.[73] It has been widely acknowledged that vertebral trabecular bone adjacent to the endplate undergoes a process of microfracture and healing during the process of spinal degeneration.[74] Cadaveric thoracolumbar spine specimens were used in mechanical experiments, which demonstrated that, in upright postures, disc degeneration results in transfer of compressive load bearing from the anterior vertebral body to the neural arch. This transfer causes a reduction in trabecular architecture anteriorly.[75] A systematic review suggested that the prevalence of IVDD increases in the presence of bony stress; whether a causal relationship exists is unclear.[76] Based on the data obtained from an experimental IVDD rat model induced by needle puncture, it appears that disc degeneration is associated with regional inhomogeneity in vertebral trabecular morphology, where the convex region of the vertebrae exhibits more severe trabecular bone morphology deterioration than the concave region.[77] The human IVD experiences a perpetually intricate load-bearing microenvironment. CS-induced disc remodeling might stimulate changes in the biomechanical environment of trabecular bone. Overall, the relationship between trabecular morphology and disc degeneration is a highly complex and dynamic phenomenon that involves a variety of cellular and molecular mechanisms. However, trabecular volume represents laying down a new osteoid (bony extracellular matrix) or an attempt at new bone formation to replace lost bone (smoking-induced osteoclastogenesis). The osteoid may not yet be mineralized (osteomalacia) or, alternatively, may be subject to delayed mineralization (osteoporosis) in a smoking environment. Further research is needed to fully understand the underlying mechanisms of their interaction.

We explored the detailed mechanisms of how TT regulates the activity of DIXDC1. m[6]A can modulate mRNA biology, including folding, maturation, nuclear processing, translation, and decay.[78] Decay is the final step in mRNA metabolism, and during this process, mRNA is destabilized and degraded. We found that TT could inhibit the decay of DIXDC1 mRNA, which is METTL14 mediated.

Protein writers, erasers, and readers mediate the effects of m[6]A. Writers and erasers determine the prevalence and distribution of m[6]A, and readers mediate m[6]A-dependent functions. Reader (m[6]A-binding) proteins include the YTH family, heterogeneous nuclear ribonucleoproteins, and IGF2BPs. YTHDF1 (The YTH N^6-methyladenosine RNA binding proteins 1), YTHDF2, and YTHDC2 increase mRNA translation, while YTHDF2 and YTHDF3 promote mRNA decay. YTHDC1 is involved in alternative splicing, nuclear export, and X chromosome silencing. YTHDF1 and YTHDF2 selectively recognize the m[6]A region and regulate mRNA degradation. Interactions between mRNA and YTHDF2 result in localization of bound mRNA from the to mRNA decay sites, like processing bodies.[79] IGF2BP1–IGF2BP3 increase the stability of targeted mRNAs.[80] Although YTHDF and IGF2BPs proteins can affect mRNA metabolism, we showed that expression of almost all reader proteins was elevated; however, only IGFBP1 and IGFBP2 can directly bind with the 3′ UTR of DIXDC1. Moreover, only IGF2BP1 knockdown impacted the levels of DIXDC1 protein.

The Wnt pathway is an intracellular central signaling cascade critical for host development and many disease processes. Wnt/β-catenin signaling is a key regulator of cartilage development.[81] The effects of the Wnt pathway in IVDs have been assessed. Pizzute et al.[82] found that OE of specific Wnt factors increased glycosaminoglycan (GAG) deposition and expression of re-differentiation genes. In NPs, its activity was undetectable but upregulated after birth.[83] In chronic compression and age-induced IVD degeneration mouse models, expression of Wnt ligand decreased and β-catenin increased in NPCs.[84] Silva and Holguin[85] reported that age-related inactivation of Wnt signaling in osterix-expressing cells suppressed IVD regeneration by inhibiting progenitors and chondrocyte-like cell expansion.[85]

Wnt/β-catenin signaling has dual roles in early IVD degeneration. Abnormal activity usually impairs NPC function, decreases matrix deposition, and accelerates fibrosis. During degeneration, chondrocyte-like cells replace notochordal cells in NP tissue. Expression of β-catenin and Wnt target genes was high in chondrocyte-like cell-rich NP tissues. However, Wnt/β-catenin signaling activity can also support notochordal cell potential progenitor characteristics.[86] Hiyama et al.[87] demonstrated that tumor necrosis factor alpha (TNF-α) and Wnt/β-catenin signaling form a positive feedback loop in NPCs, resulting in cell degeneration.[87] In zebrafish, Ccd1 was identified as a positive regulator of Wnt-TCF/LEF signaling.

We found that treatment with SM04690 attenuated the IVD degeneration induced by OE of DIXDC1. Lorecivivint (SM04690), a small-molecule Wnt pathway inhibitor, induces chondrogenesis and inhibited joint destruction in rat osteoarthritis models.[88] The mechanism underlying these effects was revealed to be by inhibiting the Wnt pathway or intranuclear kinases CDC-like kinase 2 (CLK2) and dual-specificity tyrosine phosphorylation-regulated kinase 1A (DYRK1A).[89] Deshmukh et al.[90] also showed that SM04690 could inhibit Wnt pathway gene expression and NPC senescence, decreased catabolism, and induced chondrocyte-like cell differentiation. *In vivo* studies showed increased cartilage matrix and disc height in SM04690-treated rats.[90] This demonstrated that the effects of DIXDC1 on NPCs were dependent, at least in part, on activation of the Wnt pathway.

Additional work will be required to see whether CS-induced IVDD is reduced in mMCP-6/mMCP-7-null B6 mice relative to WT B6 mice. There is currently limited literature on the efficacy of TT inhibitors/shRNA in modulating biological processes that are not solely triggered by introduction of purified tryptase. This area of research is further complicated by notable variations between human tryptase inhibitors/shRNA and their equivalents in animal models. It is plausible that a particular modification, like TT inhibitor/shRNA, while effective in suppressing human proteases, may demonstrate significantly reduced activity against the corresponding endogenous protease in MCs. It is also possible that an inhibitor/shRNA designed to selectively target a human MC protease may also exhibit potent interactions with an unidentified endogenous target that is not necessarily a protease expressed by MCs. Screening TT inhibitors and direct genetic manipulations of specific genes will be important to explore the potential therapeutic approaches to CS-induced IVDD in the future. They could establish the dependence of TT and direct dependence of mRNA stability on DIXDC1 proteins in more disease-relevant models.

Collectively, these findings define the mechanisms of pathogenesis of smoking-related IVD degeneration and LBP. This may indicate avenues such as targeting MC TT for treatment of this highly prevalent condition when smokers are unable to give up smoking or general populations are exposed to air pollution. Further, it could also help develop mRNA-based therapies that target degenerative disc disease patients who are smokers.

MATERIALS AND METHODS

Mice
All mice were bred and maintained under specific pathogen-free conditions. All experiments were performed at the Centenary Institute (Camperdown, Sydney, NSW, Australia) with 6- to 8-week-old female mice. All use of animals met the requirements of the NSW Animal Research Act 1985, NSW Animal Research Regulation 2010, and Australian Code of Practice for the Care and Use of Animals for Scientific Purposes.

CS exposure
WT C57BL/6 (B6) mice were used in the study. In each experiment, mice were simultaneously exposed to the smoke of up to 12 3R4F reference cigarettes (University of Kentucky, Lexington, KY, USA) twice per day, 5 times per week for 8 and 12 weeks using a custom-designed and purpose-built nose-only, directed-flow inhalation and smoke exposure system (CH Technologies, NJ, USA) housed in a fume and laminar flow hood as described previously described.[6,7,9,11,23–27] The experiments included 10 mice per group, which were housed 3–4 mice per cage under environmentally controlled, specific pathogen-free conditions with a 14:10 h light/dark cycle for the duration of the study.

Analysis of proteomics data
To identify peptides by their fragmentation spectra, we used MaxQuant (v.1.6.6)[91] and Andromeda as a peptide search engine integrated into the MaxQuant environment. The database for reference is the mouse proteomics dataset in Uniprot with the following parameter settings: fixed modifications, carbamidomethyl (C); variable modifications, oxidation (M), acetyl (protein N-term); enzyme, semi-trypsin; maximum missed cleavages, 2; peptide charge 2+, 3+, and 4+; peptide tolerance, ±4 ppm; MS/MS tolerance, 0.4 Da. FDR with q < 0.01 was used as a filter at the protein and peptide levels, and only proteins with at least two unique peptides were included for the final report. The functional annotated and enriched analysis, including Gene Ontology (GO) term (biological process, cellular component, molecular function), KEGG,and Cluster of Orthologous Groups (COG) of proteins) was achieved by the Diamond process of eggNOG-mapper.[92] The core analysis was carried out using the default settings, with only direct relationships and experimentally observed confidence considered. The p value for the correlation between identified proteins and a given canonical pathway was calculated by Fisher's exact test.

Rat model
The rat IVDD model was built as reported previously reported; 3-month-old rats were used.[39] A total of 10 male Sprague-Dawley rats, aged 3 months, were used for the experiments *in vivo*. Five rats were injected intradiscally with recombinant human tryptase (rhTryptase), and the remaining five rats were injected intradiscally with PBS as controls. The intervertebral space was located by digital palpation. Next, a needle was affixed using a clamp so that a 5-mm tip stuck out. After cleaning the injection site with ethanol, the needle

head was inserted into the intervertebral space and held in place for 20 s to ensure puncture. The needles were inserted into the tail discs between the seventh and eighth coccygeal vertebrae (Co7/Co8) and between Co8/Co9. Each rat was injected with two discs: one for tryptase injection and another for buffer control injections. For the tryptase groups, the discs were injected intradiscally with 15 μg/mL rhTryptase, while the control animals were injected with the same amount of PBS. The same amount (2 μL) of the solution of interest was injected into the center of the NP to eliminate the influence of the injected volume.[39] After surgery, the animals were returned to a warm and clean cage and monitored until awake.

mRNA-seq

After RNA was isolated, the 3′ mRNA single-cell RNA-seq libraries were generated utilizing disposable microfluidics cartridges to co-encapsulate single cells and barcodes into sub-nanoliter droplets on a Bio-Rad ddSEQ Single-Cell Isolator. Cell lysis, barcoding, and 3′ RNA-seq libraries generated with an Illumina SureCell WTA 3′ Library Kit were prepared for NPC samples. Libraries were prepared according to the manufacturer's protocols. Libraries were then purified and sequenced on an Illumina NextSeq 550 with 68 × 75 bp paired-end reads in mid-output mode.

MeRIP-seq

Total RNA was extracted from rat NP tissues using TRIzol reagent (Thermo Fisher, MA, USA, 15596026). An Agilent 2100 Bioanalyzer (Agilent, CA, USA) and NanoDrop 2000 (Thermo Fisher) were used for determination of total RNA quality and quantity. The total cell RNA was next fragmented into ∼100-nt-long oligonucleotides in fragmentation buffer under elevated temperature using RNA fragmentation reagent (AM8740, Invitrogen). Then post-fragmentation size distribution was validated using an Agilent 2100 Bioanalyzer and Agilent RNA 6000 Kit. Magna ChIP protein A/G magnetic beads were incubated (30 min, room temperature) with an m^{6}A-specific Ab in immunoprecipitation buffer. The mixture was then incubated with the MeRIP reaction mixture (2 h, 4°C). Sequencing was performed on an Illumina Novaseq 6000 platform following the vendor's recommended protocol.

Co-immunoprecipitation

Cell samples were lysed with NP-40 lysis buffer containing proteinase and phosphatase inhibitor cocktail (20 min on ice). After cells were harvested, 50 μL Dynabeads protein G (Life Technologies, Gaithersburg, MD, USA) was incubated with 3 μg Ab (room temperature, 1 h). Then protein lysates and bead-Ab complexes were mixed and incubated (overnight, 4°C). Beads were next washed three times with lysis buffer. Bound proteins and 10% input were analyzed by SDS immunoblotting. Gels from immunoblotting were then validated by proteomics or downstream verification experiments.

ChIP

ChIP assays were performed using SimpleChIP Enzymatic Chromatin IP Kits (Cell Signaling Technology, MA, USA) following the manufacturer's instructions. Briefly, cells were fixed with formalde-hyde to cross-link histone and non-histone proteins to DNA. Then, chromatin was digested with micrococcal nuclease into 150-900-bp DNA/protein fragments. Abs against H3K4me3, H3K9me3, H3K16ac, and H3K27ac were added for immunoprecipitation. Then cross-links were reversed, and the level of enrichment of the target DNA sequence was purified, ready for PCR. Normal rabbit IgG was used as a negative control.

RNA pull-down assays

The 3′ UTR of DIXDC1 was transcribed *in vitro* using large-scale RNA production systems (Promega, USA) and labeled with Biotin using Biotin RNA Labeling Mix and T7 RNA polymerase (Roche, Switzerland). Biotinylated RNAs were then mixed with streptavidin agarose beads (Life Technologies, 4°C overnight). Cell lysates were extracted from hNPCs and incubated with purified biotinylated transcripts (1 h, 4°C, with rotation). Then streptavidin agarose beads were added to precipitate RNA-protein complexes. After washing thoroughly three times, the RNA-protein binding mixture was boiled in SDS buffer, and the eluted proteins were detected by immunoblot.

Micro-CT

The bone micro-architecture of the tibiae was assessed *ex vivo* using a MILabs U-CT system. The scanning parameters for *ex vivo* micro-CT imaging were 5-μm pixel size, 50 kV, 200 μA, 321 projections, and 0.5-mm Al filter. Micro-CT data were exported as a DICOM file for further processing. After reconstruction, the *ex vivo* micro-CT images were segmented using a global threshold. The global threshold was visually determined to optimally separate the bimodal histogram into bone and soft tissue. Trabecular and cortical volumes of interest were selected manually, and histomorphometry parameters were calculated according to the guidelines for assessment of bone microstructure in rodents using micro-CT.[93]

Safranin-O/fast green staining

Mouse and rat spine samples were fixed with 4% paraformaldehyde for 48 h and decalcified using 15% EDTA-2Na for 3 weeks. This was followed by routine histological preparation, where 3 μm thick sections were processed for safranin O/fast green staining, as we reported previously.[94] Sections were also viewed using a digital imaging workstation under polarized light (DM6000 B, Leica Microsystems). The evaluation of the IVDD was based on modified Thompson scales (Table S1).

Sample preparation for label-free proteomics

The lumbar spines of air/CS-exposed mice were harvested after euthanasia. The surrounding soft tissues, including muscle, bone, and spinal cord, were removed under a stereoscope. The intact IVDs (including NP, AF, and CEP) were isolated from the lumbar regions and minced with a scalpel, transferred to a microcentrifuge tube, and incubated in 4 M urea, 10 mM dithiothreitol, and 50 mM NH$_4$HCO$_3$ (pH 8.6), for 2 h at room temperature with gentle agitation. After sonicating and agitating, samples were centrifuged (14,000 × g, 15 min, 4°C), supernatants were collected, and total protein concentration was assessed using the BCA assay.

Label-free proteomics was carried out using LC-MS/MS. Samples (0.8 µL) were loaded onto a micro-C18 precolumn (500 µm × 2 mm, Michrom Bioresources, CA, USA) with buffer A (0.1% formic acid [FA] in water), which was then switched via a Valco 10-port valve (Dionex/Thermo Scientific, CA, USA) into the line with a frit-less nano-column (75 µm × 10 cm) containing reverse-phase C18 medium (5 µm, 200 Å Magic, Michrom Bioresources). Samples were eluted using a 120-min gradient from 2%–30% of buffer B (98% acetonitrile, 0.1% FA, 2% H_2O) at a flow rate of 250 nL/min. Mass spectra were obtained from a linear trap quadropole (LTQ) Orbitrap Velos mass spectrometer (Thermo Electron, Bremen, Germany) in data-dependent acquisition mode in the m/z range from 350–1,750 (resolution = 30,000 at m/z 400 with an accumulation target value of 1,000,000 ions). Peptide fragmentation within the ion trap was caused by higher-energy collision dissociation, and an activation q of 0.25 and activation time of 30 ms were applied at a target value of 30,000 ions.

Culture of hNPCs

Human NP tissues from IVDs L2–S1 were isolated under a microscope. Tissue pieces were cut into 0.1 × 0.1 mm³ fragments in a sterile Petri dish, and blood was rinsed away with sterile control. Briefly, tissue samples were first washed with PBS, minced into small pieces (~1 mm³) on ice, and enzymatically digested with 500 U/mL collagenase I, 150 U/mL collagenase II, 50 U/mL collagenase IV, 0.1 mg/mL hyaluronidase, 30 U/mL DNaseI, and 5% fetal bovine serum (Oringin) for 95 min at 37°C with agitation. After centrifugation, cells were resuspended and seeded in monolayer culture with DMEM containing 10% fetal bovine serum (FBS; Gibco) and 1% penicillin-streptomycin (Sigma) and incubated (37°C, 21% O_2, and 5% CO_2).

FISH and immunofluorescence (IF)

A locked nucleic acid-modified oligonucleotide probe targeting the 3′ UTR of DIXDC1 was used for RNA FISH. The METTL14 protein *in situ* was detected with anti-METTL14 Ab (Proteintech, 26158-1-AP) using IF assays. Images were captured with a confocal microscope (Leica, Wetzlar, Germany). DAPI was used to label nuclear DNA (shown in blue). The co-localization ratio was calculated with the Co-localization Finder program of the ImageJ software. Pearson's correlation and overlap coefficient were used for quantitation.

Histopathology and IF

For immunohistochemical staining, sections were exposed to primary anti-DIXDC1 Ab (Abcam, ab226210, 1:450) and anti-METTL14 polyclonal Ab (Proteintech, 26158-1-AP, 1:150) overnight. Slides were then treated with goat anti-mouse IgG H&L (Abcam, ab205719) for slides exposed to tryptase primary Ab and polyperoxidase-conjugated anti-mouse rabbit IgG for slides stained with primary Abs against DIXDC1 and METTL14. Sections were developed in diaminobenzidine solution (Biocare Medical, Pacheco, CA, USA) under a microscope and counterstained with hematoxylin. Primary Abs were omitted for negative controls, and tissues from tonsils were used as the positive control for tryptase staining. Tissues from mouse pancreas were used as the positive control for DIXDC1 stain-

ing, and tissues from mouse testis were used as the positive control for METTL14 staining. Two pathologists, blinded to clinical information, evaluated the staining of each specimen using a semi-quantitative immunoreactivity scoring system determined by the proportion of squares occupied by immunoreactive cells compared with the stromal area in a high-power field (scale, 0–100). In case of disagreement, slides were reviewed, and a consensus was reached by the two observers.

LC-MS/MS analysis of m⁶A levels

Total RNA was extracted from rat NP tissues using TRIzol reagent (Thermo Fisher, 15596026). Next, mRNA was purified from total RNA using the NEBNext Poly(A) mRNA Magnetic Isolation Module. After digestion and centrifugation, supernatants were injected into an LC-MS/MS instrument. Nucleosides were separated and detected in positive ion multiple reaction monitoring (MRM) mode. Quantitation of modifications was determined by nucleoside-to-base ion mass transitions (m⁶A, 282 to 150; A, 268 to 136).

SA-β-gal staining

SA-β-gal staining of hNPCs was performed utilizing an SA-β-gal staining kit (Beyotime, C0602). Briefly, challenged hNPCs were fixed with 0.2% glutaraldehyde (15 min, room temperature). After washing with PBS, cells were stained with freshly prepared X-gal staining solution (pH 6.0, 37°C, overnight). After overnight incubation, cells were washed with PBS and visualized under a microscope.

RNA FISH and IF co-staining

A locked nucleic acid-modified oligonucleotide probe targeting the 3′ UTR of DIXDC1 was used for RNA FISH. The levels of METTL14 protein *in situ* were detected with anti-METTL14 Ab (Proteintech, 26158-1-AP) using IF assays. Images were captured with a confocal microscope (Leica, Wetzlar, Germany), and DAPI was used for labeling nuclear DNA (shown in blue). The co-localization ratio was calculated with Colocalization Finder of the ImageJ software, and Pearson's correlation and overlap coefficient were used for quantitation.

RIP assays

hNPCs (passage 2) were harvested and treated with formaldehyde to cross-link *in vivo* protein-RNA complexes. Cells were centrifugated (2,500 × g, 15 min) to pellet nuclei and resuspended in freshly prepared RIP buffer. Then magnetic beads coated with 5 µg of specific Abs against IgG (17–700, Millipore) or METTL14 (Proteintech, 26158-1-AP) were incubated with prepared cell lysates (overnight, 4°C). After RNA IP, RNA-protein complexes were washed 6 times and incubated with proteinase K digestion buffer. RNA was then extracted by TRIzol reagent (Thermo Fisher, 15596026). The relative interaction between METTL14 and the 3′ UTR of DIXDC1 was determined by qRT-PCR and normalized to the input.

Plasmid transfection

Stable knockdown of DIXDC1 or METTL14 was performed using CMV enhancer plasmids containing DIXDC1 or METTL14 sequences resistant to the specific shRNAs. The plasmid was designed

and assembled by Genechem Technologies. Transfections were performed with the plasmid-lipid complex using Lipofectamine 2000 (Thermo Scientific) according to the manufacturer's protocol. After 72 h, transfected cells were subjected to quantitative real-time PCR to confirm expression of DIXDC1 or METTL14 and collected for the following assay. All shRNA sequences are listed in Table S7.

siRNA transfection
To achieve IGF2BF1 and IGF2BP2 knockdown, we used Lipofectamine 2000 (Thermo Scientific) according to the protocol for 72 h with 100 nM IGF2BF1 and IGF2BP2 siRNA(GenePharma) or control. All siRNA sequences are listed in Table S7.

qRT-PCR
Total RNA was harvested from NPCs and reverse transcribed into cDNA with the PrimeScript RT Reagent Kit (Takara). Then cDNAs were subjected to qPCR analysis with FastStart SYBR Green Master Mix (Roche) and a LightCycler 96 (Roche). GAPDH was used as an internal control. For MeRIP-qPCR, qRT-PCR was carried out by our following m^6A IP to quantify changes to m^6A methylation of a certain target gene. The process for MeRIP was as described previously.[95]

RNA stability assay
To inhibit mRNA transcription, cells were treated with 5 μg/mL Actinomycin D (A1410, Sigma-Aldrich). Cells were collected at 0, 3, and 6 h, and RNA was extracted to analyze degradation rates. The mRNA half-life (t1/2) was calculated by qRT-PCR.

Protein and RNA structure prediction
The protein structure of METTL14 was predicted and analyzed by the Rosetta software package[52,53] and Alphafold.[54]

Luciferase assays
hNPCs were plated into 24-well plates at 1×10^5 cells/well density. Cells were transfected per well with 0.8 μg of shRNA plasmid together with 50 ng of SuperTOPFLASH (Beyotine, D2505) and 10 ng of pRL-TK using Lipofectamine 2000 (Thermo Scientific) for 24 h. Then transfected cells were stimulated with Wnt3a-conditioned medium for 16 h. The TCF reporter activity was measured using the Dual-Luciferase Assay System (Promega).

Statistical analysis
All data were analyzed using Prism 9 (GraphPad, USA). Comparisons of two groups were performed using unpaired Student's t test, while comparisons of three or more groups were performed using one-way ANOVA with Tukey's post hoc test. Statistical significance was accepted at $p < 0.05$. The modified Thompson scores for the histology of mouse IVDs were analyzed by Ridit analysis (**$p \leq 0.01$).

DATA AVAILABILITY
All data relevant to the study are included in the article or uploaded as supplemental information.

AUTHOR CONTRIBUTIONS
J.T., W.L., C.Y., J.Z., and A.Diwan conceived the study. J.T. and W.L. conducted all experiments and analyses. P.M.H. and C.D. provided the mouse models and revised the manuscript. X.B. provided insights and participated in proteomics analyses. A.Das helped design the study and provided critical insights into the manuscript. J.Z. contributed to funding and clinical samples and helped with animal experiments. A.Diwan organized the collaborations. All authors contributed to the writing and revising of the manuscript.

DECLARATION OF INTERESTS
The authors declare no competing interests.

REFERENCES
1. Bilano, V., Gilmour, S., and Moffiet, T. (2015). Global Trends and Projections for Tobacco Use, 1990-2025: An Analysis of Smoking Indicators From the WHO Comprehensive Information Systems for Tobacco Control. J. Vasc. Surg. 62, 1370. https://doi.org/10.1016/j.jvs.2015.09.012.

2. Ferreira, P.H., Beckenkamp, P., Maher, C.G., Hopper, J.L., and Ferreira, M.L. (2013). Nature or nurture in low back pain? Results of a systematic review of studies based on twin samples. Eur. J. Pain 17, 957–971. https://doi.org/10.1002/j.1532-2149.2012.00277.x.

3. Goldberg, M.S., Scott, S.C., and Mayo, N.E. (2000). A review of the association between cigarette smoking and the development of nonspecific back pain and related outcomes. Spine (Phila Pa 1976) 25, 995–1014. https://doi.org/10.1097/00007632-200004150-00016.

4. Nemoto, Y., Matsuzaki, H., Tokuhasi, Y., Okawa, A., Uematu, Y., Nishimura, T., and Oda, H. (2006). Histological changes in intervertebral discs after smoking and cessation: experimental study using a rat passive smoking model. J. Orthop. Sci. 11, 191–197. https://doi.org/10.1007/s00776-005-0987-4.

5. Hooten, W.M., Vickers, K.S., Shi, Y., Ebnet, K.L., Townsend, C.O., Patten, C.A., and Warner, D.O. (2011). Smoking cessation and chronic pain: patient and pain medicine physician attitudes. Pain Pract. 11, 552–563. https://doi.org/10.1111/j.1533-2500.2011.00462.x.

6. Hansbro, P.M., Hamilton, M.J., Fricker, M., Gellatly, S.L., Jarnicki, A.G., Zheng, D., Frei, S.M., Wong, G.W., Hamadi, S., Zhou, S., et al. (2014). Importance of mast cell Prss31/transmembrane tryptase/tryptase-γ in lung function and experimental chronic obstructive pulmonary disease and colitis. J. Biol. Chem. 289, 18214–18227. https://doi.org/10.1074/jbc.M114.548594.

7. Beckett, E.L., Stevens, R.L., Jarnicki, A.G., Kim, R.Y., Hanish, I., Hansbro, N.G., Deane, A., Keely, S., Horvat, J.C., Yang, M., et al. (2013). A new short-term mouse model of chronic obstructive pulmonary disease identifies a role for mast cell tryptase in pathogenesis. J. Allergy Clin. Immunol. 131, 752–762. https://doi.org/10.1016/j.jaci.2012.11.053.

8. Prieto-García, A., Zheng, D., Adachi, R., Xing, W., Lane, W.S., Chung, K., Anderson, P., Hansbro, P.M., Castells, M., and Stevens, R.L. (2012). Mast cell restricted mouse and human tryptase·heparin complexes hinder thrombin-induced coagulation of plasma and the generation of fibrin by proteolytically destroying fibrinogen. J. Biol. Chem. 287, 7834–7844. https://doi.org/10.1074/jbc.M111.325712.

9. Liu, G., Jarnicki, A.G., Paudel, K.R., Lu, W., Wadhwa, R., Philp, A.M., Van Eeckhoutte, H., Marshall, J.E., Malyla, V., Katsifis, A., et al. (2022). Adverse roles of mast cell chymase-1 in chronic obstructive pulmonary disease. Eur. Respir. J. 60, 2101431. https://doi.org/10.1183/13993003.01431-2021.

10. Tiotiu, A., Badi, Y., Kermani, N.Z., Sanak, M., Kolmert, J., Wheelock, C.E., Hansbro, P.M., Dahlén, S.E., Sterk, P.J., Djukanovic, R., et al.; U-BIOPRED Consortium Project Team (2022). Association of Differential Mast Cell Activation with Granulocytic Inflammation in Severe Asthma. Am. J. Respir. Crit. Care Med. 205, 397–411. https://doi.org/10.1164/rccm.202102-0355OC.

11. Schanin, J., Gebremeskel, S., Korver, W., Falahati, R., Butuci, M., Haw, T.J., Nair, P.M., Liu, G., Hansbro, N.G., Hansbro, P.M., et al. (2021). A monoclonal antibody to Siglec-8 suppresses non-allergic airway inflammation and inhibits IgE-independent mast cell activation. Mucosal Immunol. 14, 366–376. https://doi.org/10.1038/s41385-020-00336-9.

12. Wang, Q., Lepus, C.M., Raghu, H., Reber, L.L., Tsai, M.M., Wong, H.H., von Kaeppler, E., Lingampalli, N., Bloom, M.S., Hu, N., et al. (2019). IgE-mediated mast cell activation promotes inflammation and cartilage destruction in osteoarthritis. Elife 8, e39905. https://doi.org/10.7554/eLife.39905.

13. Stevens, R.L., McNeil, H.P., Wensing, L.A., Shin, K., Wong, G.W., Hansbro, P.M., and Krilis, S.A. (2017). Experimental Arthritis Is Dependent on Mouse Mast Cell Protease-5. J. Biol. Chem. 292, 5392–5404. https://doi.org/10.1074/jbc.M116.773416.

14. Pallaoro, M., Fejzo, M.S., Shayesteh, L., Blount, J.L., and Caughey, G.H. (1999). Characterization of genes encoding known and novel human mast cell tryptases on chromosome 16p13.3. J. Biol. Chem. 274, 3355–3362. https://doi.org/10.1074/jbc.274.6.3355.

15. McNeil, H.P., Adachi, R., and Stevens, R.L. (2007). Mast cell-restricted tryptases: structure and function in inflammation and pathogen defense. J. Biol. Chem. 282, 20785–20789. https://doi.org/10.1074/jbc.R700017200.

16. Magarinos, N.J., Bryant, K.J., Fosang, A.J., Adachi, R., Stevens, R.L., and McNeil, H.P. (2013). Mast cell-restricted, tetramer-forming tryptases induce aggrecanolysis in articular cartilage by activating matrix metalloproteinase-3 and -13 zymogens. J. Immunol. 191, 1404–1412. https://doi.org/10.4049/jimmunol.1300856.

17. Fraga, M.F., Ballestar, E., Paz, M.F., Ropero, S., Setien, F., Ballestar, M.L., Heine-Suñer, D., Cigudosa, J.C., Urioste, M., Benitez, J., et al. (2005). Epigenetic differences arise during the lifetime of monozygotic twins. Proc. Natl. Acad. Sci. USA 102, 10604–10609. https://doi.org/10.1073/pnas.0500398102.

18. Xiao, L., Hu, B., Ding, B., Zhao, Q., Liu, C., Öner, F.C., and Xu, H. (2022). N(6)-methyladenosine RNA methyltransferase like 3 inhibits extracellular matrix synthesis of endplate chondrocytes by downregulating sex-determining region Y-Box transcription factor 9 expression under tension. Osteoarthritis Cartilage 30, 613–625. https://doi.org/10.1016/j.joca.2022.01.002.

19. Zhu, B., Chen, H.X., Li, S., Tan, J.H., Xie, Y., Zou, M.X., Wang, C., Xue, J.B., Li, X.L., Cao, Y., and Yan, Y.G. (2021). Comprehensive analysis of N6-methyladenosine (m(6)A) modification during the degeneration of lumbar intervertebral disc in mice. J. Orthop. Translat. 31, 126–138. https://doi.org/10.1016/j.jot.2021.10.008.

20. Kupsco, A., Gonzalez, G., Baker, B.H., Knox, J.M., Zheng, Y., Wang, S., Chang, D., Schwartz, J., Hou, L., Wang, Y., and Baccarelli, A.A. (2020). Associations of smoking and air pollution with peripheral blood RNA N(6)-methyladenosine in the Beijing truck driver air pollution study. Environ. Int. 144, 106021. https://doi.org/10.1016/j.envint.2020.106021.

21. Cheng, C., Wu, Y., Xiao, T., Xue, J., Sun, J., Xia, H., Ma, H., Lu, L., Li, J., Shi, A., et al. (2021). METTL3-mediated m6A modification of ZBTB4 mRNA is involved in the smoking-induced EMT in cancer of the lung. Mol. Ther. Nucleic Acids 23, 487–500. https://doi.org/10.1016/j.omtn.2020.12.001.

22. Suphakhong, K., Terashima, M., Wanna-Udom, S., Takatsuka, R., Ishimura, A., Takino, T., and Suzuki, T. (2022). m6A RNA methylation regulates the transcription factors JUN and JUNB in TGF-β-induced epithelial-mesenchymal transition of lung cancer cells. J. Biol. Chem. 298, 102554. https://doi.org/10.1016/j.jbc.2022.102554.

23. Fricker, M., Goggins, B.J., Mateer, S., Jones, B., Kim, R.Y., Gellatly, S.L., Jarnicki, A.G., Powell, N., Oliver, B.G., Radford-Smith, G., et al. (2018). Chronic cigarette smoke exposure induces systemic hypoxia that drives intestinal dysfunction. JCI Insight 3, e94040. https://doi.org/10.1172/jci.insight.94040.

24. Starkey, M.R., Plank, M.W., Casolari, P., Papi, A., Pavlidis, S., Guo, Y., Cameron, G.J.M., Haw, T.J., Tam, A., Obiedat, M., et al. (2019). IL-22 and its receptors are increased in human and experimental COPD and contribute to pathogenesis. Eur. Respir. J. 54, 1800174. https://doi.org/10.1183/13993003.00174-2018.

25. Lu, Z., Van Eeckhoutte, H.P., Liu, G., Nair, P.M., Jones, B., Gillis, C.M., Nalkurthi, B.C., Verhamme, F., Buyle-Huybrecht, T., Vandenabeele, P., et al. (2021). Necroptosis Signaling Promotes Inflammation, Airway Remodeling, and Emphysema in Chronic Obstructive Pulmonary Disease. Am. J. Respir. Crit. Care Med. 204, 667–681. https://doi.org/10.1164/rccm.202009-3442OC.

26. Kim, R.Y., Sunkara, K.P., Bracke, K.R., Jarnicki, A.G., Donovan, C., Hsu, A.C., Ieni, A., Beckett, E.L., Galvão, I., Wijnant, S., et al. (2021). A microRNA-21-mediated SATB1/S100A9/NF-κB axis promotes chronic obstructive pulmonary disease pathogenesis. Sci. Transl. Med. 13, eaav7223. https://doi.org/10.1126/scitranslmed.aav7223.

27. Donovan, C., Kim, R.Y., Galvao, I., Jarnicki, A.G., Brown, A.C., Jones-Freeman, B., Gomez, H.M., Wadhwa, R., Hortle, E., Jayaraman, R., et al. (2022). Aim2 suppresses cigarette smoke-induced neutrophil recruitment, neutrophil caspase-1 activation and anti-Ly6G-mediated neutrophil depletion. Immunol. Cel Biol. 100, 235–249. https://doi.org/10.1111/imcb.12537.

28. Jones, B., Donovan, C., Liu, G., Gomez, H.M., Chimankar, V., Harrison, C.L., Wiegman, C.H., Adcock, I.M., Knight, D.A., Hirota, J.A., and Hansbro, P.M. (2017). Animal models of COPD: What do they tell us? Respirology 22, 21–32. https://doi.org/10.1111/resp.12908.

29. Kushchayev, S.V., Glushko, T., Jarraya, M., Schuleri, K.H., Preul, M.C., Brooks, M.L., and Teytelboym, O.M. (2018). ABCs of the degenerative spine. Insights Imaging 9, 253–274. https://doi.org/10.1007/s13244-017-0584-z.

30. Steck, E., Bertram, H., Abel, R., Chen, B., Winter, A., and Richter, W. (2005). Induction of intervertebral disc-like cells from adult mesenchymal stem cells. Stem Cells 23, 403–411. https://doi.org/10.1634/stemcells.2004-0107.

31. Nasto, L.A., Seo, H.-Y., Robinson, A.R., Tilstra, J.S., Clauson, C.L., Sowa, G.A., Ngo, K., Dong, Q., Pola, E., Lee, J.Y., et al. (2012). ISSLS prize winner: inhibition of NF-κB activity ameliorates age-associated disc degeneration in a mouse model of accelerated aging. Spine 37, 1819–1825. https://doi.org/10.1097/BRS.0b013e31824ee8f7.

32. Zhang, F., Zhao, X., Shen, H., and Zhang, C. (2016). Molecular mechanisms of cell death in intervertebral disc degeneration (Review). Int. J. Mol. Med. 37, 1439–1448. https://doi.org/10.3892/ijmm.2016.2573.

33. Sun, L., Gooding, H.L., Brunton, P.J., Russell, J.A., Mitchell, R., and Fleetwood-Walker, S. (2013). Phospholipase D-mediated hypersensitivity at central synapses is associated with abnormal behaviours and pain sensitivity in rats exposed to prenatal stress. Int. J. Biochem. Cel Biol. 45, 2706–2712. https://doi.org/10.1016/j.biocel.2013.07.017.

34. Chédotal, A. (2019). Roles of axon guidance molecules in neuronal wiring in the developing spinal cord. Nat. Rev. Neurosci. 20, 380–396. https://doi.org/10.1038/s41583-019-0168-7.

35. Mi, H., Ebert, D., Muruganujan, A., Mills, C., Albou, L.P., Mushayamaha, T., and Thomas, P.D. (2021). PANTHER version 16: a revised family classification, tree-based classification tool, enhancer regions and extensive API. Nucleic Acids Res. 49, D394–D403. https://doi.org/10.1093/nar/gkaa1106.

36. Habtemariam, A., Virri, J., Grönblad, M., Seitsalo, S., and Karaharju, E. (1999). The role of mast cells in disc herniation inflammation. Spine (Phila Pa 1976) 24, 1516–1520. https://doi.org/10.1097/00007632-199908010-00003.

37. Andersson, C.K., Mori, M., Bjermer, L., Löfdahl, C.G., and Erjefält, J.S. (2010). Alterations in lung mast cell populations in patients with chronic obstructive pulmonary disease. Am. J. Respir. Crit. Care Med. 181, 206–217. https://doi.org/10.1164/rccm.200906-0932OC.

38. Ballarin, A., Bazzan, E., Zenteno, R.H., Turato, G., Baraldo, S., Zanovello, D., Mutti, E., Hogg, J.C., Saetta, M., and Cosio, M.G. (2012). Mast cell infiltration discriminates between histopathological phenotypes of chronic obstructive pulmonary disease. Am. J. Respir. Crit. Care Med. 186, 233–239. https://doi.org/10.1164/rccm.201112-2142OC.

39. Mao, H.J., Chen, Q.X., Han, B., Li, F.C., Feng, J., Shi, Z.L., Lin, M., and Wang, J. (2011). The effect of injection volume on disc degeneration in a rat tail model. Spine 36, E1062–E1069. https://doi.org/10.1097/BRS.0b013e3182027d42.

40. Lai, A., Gansau, J., Gullbrand, S.E., Crowley, J., Cunha, C., Dudli, S., Engiles, J.B., Fusellier, M., Goncalves, R.M., Nakashima, D., et al. (2021). Development of a standardized histopathology scoring system for intervertebral disc degeneration in rat models: An initiative of the ORS spine section. JOR SPINE 4, e1150. https://doi.org/10.1002/jsp2.1150.

41. Zaccara, S., Ries, R.J., and Jaffrey, S.R. (2019). Reading, writing and erasing mRNA methylation. Nat. Rev. Mol. Cel Biol. 20, 608–624. https://doi.org/10.1038/s41580-019-0168-5.

42. Wang, X., Chen, N., Du, Z., Ling, Z., Zhang, P., Yang, J., Khaleel, M., Khoury, A.N., Li, J., Li, S., et al. (2020). Bioinformatics analysis integrating metabolomics of m(6)A RNA microarray in intervertebral disc degeneration. Epigenomics 12, 1419–1441. https://doi.org/10.2217/epi-2020-0101.

43. Tu, J., Li, W., Yang, S., Yang, P., Yan, Q., Wang, S., Lai, K., Bai, X., Wu, C., Ding, W., et al. (2022). Single-Cell Transcriptome Profiling Reveals Multicellular Ecosystem of Nucleus Pulposus during Degeneration Progression. Adv. Sci. 9, e2103631. https://doi.org/10.1002/advs.202103631.

44. Martin, P.M., Stanley, R.E., Ross, A.P., Freitas, A.E., Moyer, C.E., Brumback, A.C., Iafrati, J., Stapornwongkul, K.S., Dominguez, S., Kivimäe, S., et al. (2018). DIXDC1 contributes to psychiatric susceptibility by regulating dendritic spine and glutamatergic synapse density via GSK3 and Wnt/β-catenin signaling. Mol. Psychiatry 23, 467–475. https://doi.org/10.1038/mp.2016.184.

45. Cully, M. (2013). Degenerative disc disease: Altered Wnt signalling in intervertebral disc degeneration. Nat. Rev. Rheumatol. 9, 136. https://doi.org/10.1038/nrrheum.2013.22.

46. Holguin, N., Aguilar, R., Harland, R.A., Bomar, B.A., and Silva, M.J. (2014). The aging mouse partially models the aging human spine: lumbar and coccygeal disc height, composition, mechanical properties, and Wnt signaling in young and old mice. J. Appl. Physiol. 116, 1551–1560. https://doi.org/10.1152/japplphysiol.01322.2013.

47. Skvortsova, K., Iovino, N., and Bogdanović, O. (2018). Functions and mechanisms of epigenetic inheritance in animals. Nat. Rev. Mol. Cel Biol. 19, 774–790. https://doi.org/10.1038/s41580-018-0074-2.

48. Huang, H., Weng, H., Zhou, K., Wu, T., Zhao, B.S., Sun, M., Chen, Z., Deng, X., Xiao, G., Auer, F., et al. (2019). Histone H3 trimethylation at lysine 36 guides m(6)A RNA modification co-transcriptionally. Nature 567, 414–419. https://doi.org/10.1038/s41586-019-1016-7.

49. Zheng, R., Wan, C., Mei, S., Qin, Q., Wu, Q., Sun, H., Chen, C.-H., Brown, M., Zhang, X., Meyer, C.A., and Liu, X.S. (2019). Cistrome Data Browser: expanded datasets and new tools for gene regulatory analysis. Nucleic Acids Res. 47, D729–D735. https://doi.org/10.1093/nar/gky1094.

50. Kent, W.J., Sugnet, C.W., Furey, T.S., Roskin, K.M., Pringle, T.H., Zahler, A.M., and Haussler, D. (2002). The human genome browser at UCSC. Genome Res. 12, 996–1006. https://doi.org/10.1101/gr.229102.

51. Zhou, Y., Zeng, P., Li, Y.H., Zhang, Z., and Cui, Q. (2016). SRAMP: prediction of mammalian N6-methyladenosine (m6A) sites based on sequence-derived features. Nucleic Acids Res. 44, e91. https://doi.org/10.1093/nar/gkw104.

52. Bradley, P., Misura, K.M.S., and Baker, D. (2005). Toward high-resolution de novo structure prediction for small proteins. Science 309, 1868–1871. https://doi.org/10.1126/science.1113801.

53. Kaufmann, K.W., Lemmon, G.H., Deluca, S.L., Sheehan, J.H., and Meiler, J. (2010). Practically useful: what the Rosetta protein modeling suite can do for you. Biochemistry 49, 2987–2998. https://doi.org/10.1021/bi902153g.

54. Tunyasuvunakool, K., Adler, J., Wu, Z., Green, T., Zielinski, M., Žídek, A., Bridgland, A., Cowie, A., Meyer, C., Laydon, A., et al. (2021). Highly accurate protein structure prediction for the human proteome. Nature 596, 590–596. https://doi.org/10.1038/s41586-021-03828-1.

55. Lorenz, R., Bernhart, S.H., Höner Zu Siederdissen, C., Tafer, H., Flamm, C., Stadler, P.F., and Hofacker, I.L. (2011). ViennaRNA Package 2.0. Algorithms Mol. Biol. 6, 26. https://doi.org/10.1186/1748-7188-6-26.

56. Patil, D.P., Pickering, B.F., and Jaffrey, S.R. (2018). Reading m(6)A in the Transcriptome: m(6)A-Binding Proteins. Trends Cel Biol. 28, 113–127. https://doi.org/10.1016/j.tcb.2017.10.001.

57. Huang, H., Weng, H., Sun, W., Qin, X., Shi, H., Wu, H., Zhao, B.S., Mesquita, A., Liu, C., Yuan, C.L., et al. (2018). Recognition of RNA N(6)-methyladenosine by IGF2BP proteins enhances mRNA stability and translation. Nat. Cel Biol. 20, 285–295. https://doi.org/10.1038/s41556-018-0045-z.

58. Shiomi, K., Uchida, H., Keino-Masu, K., and Masu, M. (2003). Ccd1, a novel protein with a DIX domain, is a positive regulator in the Wnt signaling during zebrafish neural patterning. Curr. Biol. 13, 73–77. https://doi.org/10.1016/s0960-9822(02)01398-2.

59. Singh, K.K., Ge, X., Mao, Y., Drane, L., Meletis, K., Samuels, B.A., and Tsai, L.H. (2010). Dixdc1 is a critical regulator of DISC1 and embryonic cortical development. Neuron 67, 33–48. https://doi.org/10.1016/j.neuron.2010.06.002.

60. Huang, C., De Sanctis, G.T., O'Brien, P.J., Mizgerd, J.P., Friend, D.S., Drazen, J.M., Brass, L.F., and Stevens, R.L. (2001). Evaluation of the substrate specificity of human mast cell tryptase beta I and demonstration of its importance in bacterial infections of the lung. J. Biol. Chem. 276, 26276–26284. https://doi.org/10.1074/jbc.M102356200.

61. Huang, C., Friend, D.S., Qiu, W.T., Wong, G.W., Morales, G., Hunt, J., and Stevens, R.L. (1998). Induction of a selective and persistent extravasation of neutrophils into the peritoneal cavity by tryptase mouse mast cell protease 6. J. Immunol. 160, 1910–1919.

62. Briggaman, R.A., Schechter, N.M., Fraki, J., and Lazarus, G.S. (1984). Degradation of the epidermal-dermal junction by proteolytic enzymes from human skin and human polymorphonuclear leukocytes. J. Exp. Med. 160, 1027–1042. https://doi.org/10.1084/jem.160.4.1027.

63. Gruber, B.L., Marchese, M.J., Suzuki, K., Schwartz, L.B., Okada, Y., Nagase, H., and Ramamurthy, N.S. (1989). Synovial procollagenase activation by human mast cell tryptase dependence upon matrix metalloproteinase 3 activation. J. Clin. Invest. 84, 1657–1662. https://doi.org/10.1172/jci114344.

64. Abe, M., Kurosawa, M., Ishikawa, O., Miyachi, Y., and Kido, H. (1998). Mast cell tryptase stimulates both human dermal fibroblast proliferation and type I collagen production. Clin. Exp. Allergy 28, 1509–1517. https://doi.org/10.1046/j.1365-2222.1998.00360.x.

65. Saarinen, J., Kalkkinen, N., Welgus, H.G., and Kovanen, P.T. (1994). Activation of human interstitial procollagenase through direct cleavage of the Leu83-Thr84 bond by mast cell chymase. J. Biol. Chem. 269, 18134–18140.

66. Cairns, J.A., and Walls, A.F. (1997). Mast cell tryptase stimulates the synthesis of type I collagen in human lung fibroblasts. J. Clin. Invest. 99, 1313–1321. https://doi.org/10.1172/jci119290.

67. Taipale, J., Lohi, J., Saarinen, J., Kovanen, P.T., and Keski-Oja, J. (1995). Human mast cell chymase and leukocyte elastase release latent transforming growth factor-beta 1 from the extracellular matrix of cultured human epithelial and endothelial cells. J. Biol. Chem. 270, 4689–4696. https://doi.org/10.1074/jbc.270.9.4689.

68. Liu, G., Cooley, M.A., Jarnicki, A.G., Borghuis, T., Nair, P.M., Tjin, G., Hsu, A.C., Haw, T.J., Fricker, M., Harrison, C.L., et al. (2019). Fibulin-1c regulates transforming growth factor-β activation in pulmonary tissue fibrosis. JCI Insight 5, e124529. https://doi.org/10.1172/jci.insight.124529.

69. Wong, C.K., Luo, W., Deng, Y., Zou, H., Ye, Z., and Lin, S.C. (2004). The DIX domain protein coiled-coil-DIX1 inhibits c-Jun N-terminal kinase activation by Axin and dishevelled through distinct mechanisms. J. Biol. Chem. 279, 39366–39373. https://doi.org/10.1074/jbc.M404598200.

70. Wang, L., Li, H., Chen, Q., Zhu, T., Zhu, H., and Zheng, L. (2010). Wnt signaling stabilizes the DIXDC1 protein through decreased ubiquitin-dependent degradation. Cancer Sci. 101, 700–706. https://doi.org/10.1111/j.1349-7006.2009.01448.x.

71. Goodwin, J.M., Svensson, R.U., Lou, H.J., Winslow, M.M., Turk, B.E., and Shaw, R.J. (2014). An AMPK-independent signaling pathway downstream of the LKB1 tumor suppressor controls Snail1 and metastatic potential. Mol. Cel 55, 436–450. https://doi.org/10.1016/j.molcel.2014.06.021.

72. Sasaki, M., Chubachi, S., Kameyama, N., Sato, M., Haraguchi, M., Miyazaki, M., Takahashi, S., Nakano, T., Kuroda, Y., Betsuyaku, T., and Matsuo, K. (2018). Effects of long-term cigarette smoke exposure on bone metabolism, structure, and quality in a mouse model of emphysema. PloS one 13, e0191611. https://doi.org/10.1371/journal.pone.0191611.

73. Ma, D., Li, Y., Hackfort, B., Zhao, Y., Xiao, J., Swanson, P.C., Lappe, J., Xiao, P., Cullen, D., Akhter, M., et al. (2012). Smoke-induced signal molecules in bone marrow cells from altered low-density lipoprotein receptor-related protein 5 mice. J. Proteome Res. 11, 3548–3560. https://doi.org/10.1021/pr2012158.

74. Vernon-Roberts, B., and Pirie, C.J. (1973). Healing trabecular microfractures in the bodies of lumbar vertebrae. Ann. Rheum. Dis. 32, 406–412. https://doi.org/10.1136/ard.32.5.406.

75. Adams, M.A., Pollintine, P., Tobias, J.H., Wakley, G.K., and Dolan, P. (2006). Intervertebral disc degeneration can predispose to anterior vertebral fractures in the thoracolumbar spine. J. Bone Miner. Res. 21, 1409–1416. https://doi.org/10.1359/jbmr.060609.

76. Chepurin, D., Chamoli, U., and Diwan, A.D. (2022). Bony Stress and Its Association With Intervertebral Disc Degeneration in the Lumbar Spine: A Systematic Review of Clinical and Basic Science Studies. Glob. Spine J. 12, 964–979. https://doi.org/10.1177/21925682211008837.

77. Ni, L., Zhang, L., Xia, W., Chen, G., Cui, X., Zhang, W., Luo, Z., and Yang, H. (2018). Disc degeneration promotes regional inhomogeneity in the trabecular morphology of loaded rat tail vertebrae. J. Orthop. Translat. 15, 104–111. https://doi.org/10.1016/j.jot.2018.07.008.

78. Zhao, B.S., Roundtree, I.A., and He, C. (2017). Post-transcriptional gene regulation by mRNA modifications. Nat. Rev. Mol. Cel Biol. 18, 31–42. https://doi.org/10.1038/nrm.2016.132.

79. Wang, X., Lu, Z., Gomez, A., Hon, G.C., Yue, Y., Han, D., Fu, Y., Parisien, M., Dai, Q., Jia, G., et al. (2014). N6-methyladenosine-dependent regulation of messenger RNA stability. Nature 505, 117–120. https://doi.org/10.1038/nature12730.

80. Zhao, Y., Shi, Y., Shen, H., and Xie, W. (2020). m6A-binding proteins: the emerging crucial performers in epigenetics. J. Hematol. Oncol. 13, 35. https://doi.org/10.1186/s13045-020-00872-8.

81. Tamamura, Y., Otani, T., Kanatani, N., Koyama, E., Kitagaki, J., Komori, T., Yamada, Y., Costantini, F., Wakisaka, S., Pacifici, M., et al. (2005). Developmental regulation of Wnt/beta-catenin signals is required for growth plate assembly, cartilage integrity, and endochondral ossification. J. Biol. Chem. 280, 19185–19195. https://doi.org/10.1074/jbc.M414275200.

82. Pizzute, T., He, F., Zhang, X.-B., and Pei, M. (2018). Impact of Wnt signals on human intervertebral disc cell regeneration. J. Orthop. Res. 36, 3196–3207. https://doi.org/10.1002/jor.24115.

83. Kondo, N., Yuasa, T., Shimono, K., Tung, W., Okabe, T., Yasuhara, R., Pacifici, M., Zhang, Y., Iwamoto, M., and Enomoto-Iwamoto, M. (2011). Intervertebral disc development is regulated by Wnt/β-catenin signaling. Spine 36, E513–E518. https://doi.org/10.1097/BRS.0b013e3181f52cb5.

84. Holguin, N., and Silva, M.J. (2018). In-Vivo Nucleus Pulposus-Specific Regulation of Adult Murine Intervertebral Disc Degeneration via Wnt/Beta-Catenin Signaling. Sci. Rep. 8, 11191. https://doi.org/10.1038/s41598-018-29352-3.

85. Silva, M.J., and Holguin, N. (2020). Aging aggravates intervertebral disc degeneration by regulating transcription factors toward chondrogenesis. FASEB J. : official Publ. Fed. Am. Societies Exp. Biol. 34, 1970–1982. https://doi.org/10.1096/fj.201902109R.

86. Smolders, L.A., Meij, B.P., Riemers, F.M., Licht, R., Wubbolts, R., Heuvel, D., Grinwis, G.C., Vernooij, H.C., Hazewinkel, H.A., Penning, L.C., and Tryfonidou, M.A. (2012). Canonical Wnt signaling in the notochordal cell is upregulated in early intervertebral disk degeneration. J. Orthop. Res. 30, 950–957. https://doi.org/10.1002/jor.22000.

87. Hiyama, A., Yokoyama, K., Nukaga, T., Sakai, D., and Mochida, J. (2013). A complex interaction between Wnt signaling and TNF-α in nucleus pulposus cells. Arthritis Res. Ther. 15, R189. https://doi.org/10.1186/ar4379.

88. Deshmukh, V., Hu, H., Barroga, C., Bossard, C., Kc, S., Dellamary, L., Stewart, J., Chiu, K., Ibanez, M., Pedraza, M., et al. (2018). A small-molecule inhibitor of the Wnt pathway (SM04690) as a potential disease modifying agent for the treatment of osteoarthritis of the knee. Osteoarthritis Cartilage 26, 18–27. https://doi.org/10.1016/j.joca.2017.08.015.

89. Deshmukh, V., O'Green, A.L., Bossard, C., Seo, T., Lamangan, L., Ibanez, M., Ghias, A., Lai, C., Do, L., Cho, S., et al. (2019). Modulation of the Wnt pathway through inhibition of CLK2 and DYRK1A by lorecivivint as a novel, potentially disease-modifying approach for knee osteoarthritis treatment. Osteoarthritis Cartilage 27, 1347–1360. https://doi.org/10.1016/j.joca.2019.05.006.

90. Deshmukh, V., Ibanez, M., Hu, H., Cahiwat, J., Wei, Y., Stewart, J., Hood, J., and Yazici, Y. (2020). A small-molecule inhibitor of the Wnt pathway, lorecivivint (SM04690), as a potential disease-modifying agent for the treatment of degenerative disc disease. Spine J. 20, 1492–1502. https://doi.org/10.1016/j.spinee.2020.04.024.

91. Cox, J., and Mann, M. (2008). MaxQuant enables high peptide identification rates, individualized p.p.b.-range mass accuracies and proteome-wide protein quantification. Nat. Biotechnol. 26, 1367–1372. https://doi.org/10.1038/nbt.1511.

92. Huerta-Cepas, J., Forslund, K., Coelho, L.P., Szklarczyk, D., Jensen, L.J., von Mering, C., and Bork, P. (2017). Fast Genome-Wide Functional Annotation through Orthology Assignment by eggNOG-Mapper. Mol. Biol. Evol. 34, 2115–2122. https://doi.org/10.1093/molbev/msx148.

93. Bouxsein, M.L., Boyd, S.K., Christiansen, B.A., Guldberg, R.E., Jepsen, K.J., and Müller, R. (2010). Guidelines for assessment of bone microstructure in rodents using micro-computed tomography. J. Bone Miner. Res. 25, 1468–1486. https://doi.org/10.1002/jbmr.141.

94. Wei, A., Williams, L.A., Bhargav, D., Shen, B., Kishen, T., Duffy, N., and Diwan, A.D. (2009). BMP13 prevents the effects of annular injury in an ovine model. Int. J. Biol. Sci. 5, 388–396. https://doi.org/10.7150/ijbs.5.388.

95. Roberts, T.C., Hart, J.R., Kaikkonen, M.U., Weinberg, M.S., Vogt, P.K., and Morris, K.V. (2015). Quantification of nascent transcription by bromouridine immunocapture nuclear run-on RT-qPCR. Nat. Protoc. 10, 1198–1211. https://doi.org/10.1038/nprot.2015.076.